min dialysate samples were collected during the initial 60-min and subsequently three consecutive samples were collected over a period of 6 h with a 2 h-interval ($n = 6$).

### 2.4. Statistical analysis

All data are presented as mean ± S.E. values. Hemodynamic and dialysate data responses to acute ischemia were statistically analyzed by analysis of variance with repeated measures. When a statistically significant effect of ischemia was detected as a whole, the Dunnett's test was applied to determine which mean values differed significantly from the control level. When a statistically significant effect of the treatment was detected, Newman–Keuls test was applied to determine which treatment differed significantly from the vehicle.

## 3. Results

Table 1 summarizes changes in HR and MAP. MAP and HR increased during 6 h-hind limb ischemia. Changes in MAP at 2 h and HR at 6 h-hind limb ischemia were significant.

### 3.1. Time courses of dialysate NE levels during short and prolonged ischemia

Skeletal muscle dialysate NE levels decreased from 19 ± 4 pg/ml at control to 9 ± 4 pg/ml at 30 min of ischemia and reached 2 ± 0 pg/ml at 60 min of ischemia (Fig. 2). The decrease in dialysate NE level was maintained after 2 h of ischemia. Then skeletal muscle dialysate NE levels markedly increased to 143 ± 30 pg/ml at 4 h of ischemia. The dialysate NE levels continued to increase progressively and reached 289 ± 45 pg/ml at 6 h of ischemia. Skeletal muscle dialysate DHPG levels decreased from 38 ± 2 pg/ml at control to 5 ± 1 pg/ml at 2 h of ischemia and reached 7 ± 1 pg/ml at 6 h of ischemia.

### 3.2. Involvement of NE uptake, transport, $Ca^{2+}$ channels and cytosol $Ca^{2+}$ in dialysate NE levels during prolonged ischemia

Dialysate NE increases at 4 and 6 h-skeletal muscle ischemia were not suppressed by treatment with desipramine (Fig. 3). Dialysate NE increases at 4 and 6 h-skeletal muscle ischemia were not suppressed by treatment with ω-conotoxin GVIA. Treatment with TMB-8 significantly suppressed the dialysate NE increase at 4 h-skeletal muscle ischemia. But at 6 h-skeletal muscle ischemia, there was no significant difference in dialysate NE levels among treatments.

Table 1
Changes in heart rate (HR) and mean arterial pressure (MAP) in 6 h-hindlimb ischemia

| | Control | 2 h | 4 h | 6 h |
|---|---|---|---|---|
| HR (beats/min) | 283 ± 10 | 292 ± 4 | 293 ± 8 | 302 ± 8* |
| MAP (mmHg) | 104 ± 6 | 114 ± 3* | 111 ± 4 | 108 ± 4 |

Values are means ± S.E. from six rabbits. Data were obtained during control, after 2, 4, and 6 h of hind limb ischemia.
* $P < 0.05$ vs. control.

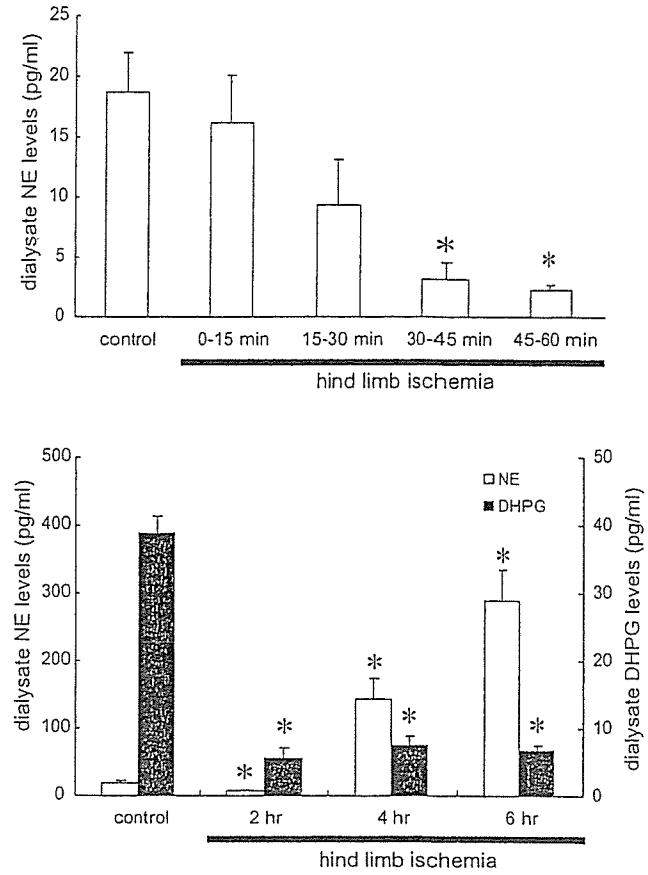


Fig. 2. (Upper panel) Time course of dialysate norepinephrine (NE) levels during 60 min-hind limb ischemia. Values are means ± S.E. ($n = 6$). *$P < 0.05$ vs. control value. (Lower panel) Time courses of dialysate NE and dihydroxyphenylglycol (DHPG) levels during 6 h-hind limb ischemia. Values are means ± S.E. ($n = 6$). *$P < 0.05$ vs. control value.

### 3.3. Time course of dialysate lactate levels during hind limb ischemia

Skeletal muscle dialysate lactate levels increased from 0.6 ± 0.07 nmol/l at control to 1.73 ± 0.17 nmol/l at 45–60 min

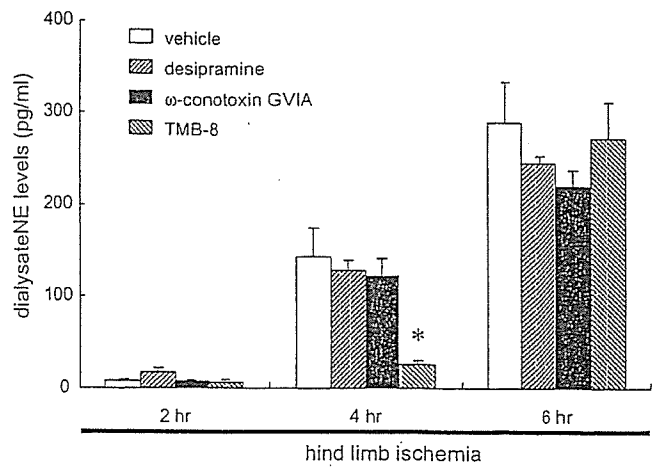


Fig. 3. Effects of pharmacological intervention on dialysate norepinephrine (NE) levels evoked by 6 h-hind limb ischemia. Desipramine (100 μM), ω-conotoxin (10 μM), or TMB-8 (1 mM) was locally administered through the probe. Values are means ± S.E. ($n = 6$). *$P < 0.05$ vs. concurrent value of vehicle group.

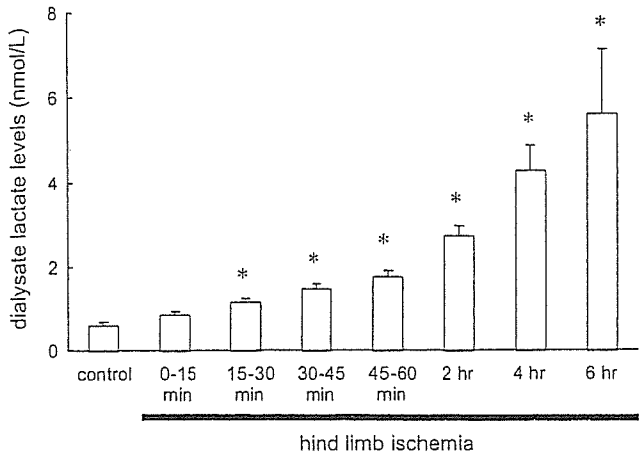


Fig. 4. Time course of dialysate lactate levels during 6 h-hind limb ischemia. Values are means ± S.E. ($n = 6$). $^*P < 0.05$ vs. control value.

of ischemia (Fig. 4). These step-wise increases were continued for 6 h of the hind limb ischemia.

## 4. Discussion

Using dialysis techniques in the in vivo rabbit skeletal muscle, we examined interstitial levels of NE in the control and ischemic period, and observed the biphasic response of dialysate NE in ischemic skeletal muscle. Ischemia induced an initial reduction followed by a progressive increment in dialysate NE levels. Here we discuss changes in interstitial NE and possible mechanisms underlying sympathetic nerve impairment.

Within 2 h of acute skeletal muscle ischemia, unlike acute myocardial ischemia, skeletal muscle interstitial NE levels continued to decline progressively, decreasing to one-tenth of control at 60 min of ischemia. A previous study demonstrated that skeletal muscle ischemia modulated the baroreflex control of regional muscle sympathetic activity (Cornett et al., 2000). At 75 min of acute skeletal muscle ischemia, hemodynamic responses to carotid occlusion were preserved while the interstitial NE response to carotid occlusion was blunted in the ischemic region (Tokunaga et al., 2003b). These results indicate that the systemic response to baroreflex remained intact while the skeletal muscle sympathetic response was impaired in ischemic regions. Earlier studies reported that acute limb ischemia reduced the conduction of motor nerves such as sciatic nerve (Fern and Harrison, 1994), and induced axonal degeneration histologically (Makitie and Teravainen, 1977; Nukada and Dyek, 1987). Axonal conduction in the ischemic muscle sympathetic nerve may be impaired as well as in sensory and motor nerves. In addition to diminished axonal conductance, the interstitial NE response to high $K^+$ but not tyramine was suppressed during the 75 min of acute skeletal muscle ischemia, although NE content at muscle sympathetic nerve endings was preserved during the ischemia (Tokunaga et al., 2003b). This result indicates that exocytotic NE releasing function in muscle sympathetic nerve endings might be suppressed during 75 min of acute skeletal muscle ischemia. Therefore, initial reduction of NE release may be mediated by an impairment of axonal conduction and/or NE releasing function.

After 2 h of acute skeletal muscle ischemia, skeletal muscle interstitial NE levels significantly increased and finally reached 20-fold that of control. This amount of NE release is higher than that evoked by baroreflex or high $K^+$. This level is similar to that evoked by the $Na^+$–$K^+$ ATPase inhibitor, ouabain (Tokunaga et al., 2003a). The amount of NE release evoked by ischemia may be dependent on the density of sympathetic innervation. Dispersed organ systems such as skeletal muscle have a thin and diffuse sympathetic innervation. This is the first report to describe that marked NE release is induced from muscle sympathetic nerve endings in the ischemic region after 2 h of skeletal muscle ischemia. Numerous histological changes of skeletal muscle have been reported after ischemia and reperfusion injury (Patterson and Klenerman, 1979; Turchányi et al., 2005). However, there is no histochemical evidence of the impaired sympathetic nerves in the skeletal muscle ischemia.

In the case of skeletal muscle ischemia, ω-conotoxin GVIA did not suppress NE efflux. N-type $Ca^{2+}$ channels are not involved in this NE efflux. Desipramine did not alter NE efflux during skeletal muscle ischemia. Desipramine inhibits carrier-mediated NE transport in both directions. Considering that desipramine did not alter interstitial NE levels, the amounts of NE release and uptake via normal transport can be surmised to be negligible. Second, the increase in skeletal muscle interstitial NE levels was not associated with an increase in skeletal muscle interstitial DHPG levels, indicating that skeletal ischemia fails to induce axoplasmic NE elevation via alterations in monoamine activity, NE mobilization from stored vesicle, and NE uptake. Further, desipramine did not suppress NE efflux. These results exclude the possibility that marked increases in skeletal muscle interstitial NE could be due to carrier-mediated outward transport of NE for removal of elevated axoplasmic NE concentration. The membrane NE transporter exists in the skeletal muscle sympathetic nerve endings (Cabassi et al., 2001; Tokunaga et al., 2003a), but was not involved in outward transport of NE. Thus, we consider that a ω-conotoxin GVIA insensitive and desipramine-resistant NE release mechanism exists after 2 h of acute skeletal muscle ischemia.

TMB-8 significantly suppressed the marked NE release at 4 h of skeletal muscle ischemia. TMB-8 is well known to inhibit $Ca^{2+}$ release from intracellular $Ca^{2+}$ stores. TMB-8 inhibits caffeine-induced catecholamine release from perfused adrenal gland in the absence of extracellular $Ca^{2+}$ (Yamada et al., 1988). Studies using chromaffin cells, brain slices and synaptosomes have suggested that metabolic inhibition induces intracellular $Ca^{2+}$ overload (Milusheva et al., 1992), and a rise in the intracellular $Ca^{2+}$ causes exocytotic catecholamine release without membrane depolarization (Dry et al., 1991; Du et al., 1997). Moreover, an in vitro study with adrenergic nerves of guinea-pig vas deferens suggested that $Ca^{2+}$ release from intracellular $Ca^{2+}$ stores is to some extent involved in the NE release evoked by elevation of intracellular $Na^+$ (Katsuragi et al., 1994). Under energy-depleted conditions, $Ca^{2+}$ overload

in synaptosomes of noradrenergic neurons from the brain is an important mechanism for the enhanced release of neurotransmitter, with a reversal of $Na^+$–$Ca^{2+}$ exchange possibly the key pathway leading to intraneuronal $Ca^{2+}$ overload (Du et al., 1997). We consider that $Ca^{2+}$ release from intracellular $Ca^{2+}$ stores is partly involved in the NE release at 4 h of skeletal muscle ischemia.

At 6 h of skeletal ischemia, increment in dialysate NE level was not suppressed by the pretreatments. This result suggests that another mechanism may be involved in NE release, which is insensitive to desipramine, ω-conotoxin GVIA, and TMB-8. Alternatively, the NE release may occur with development of irreversible membrane damage and can no longer be inhibited by pharmacological interventions. Future work should concentrate on these aspects of NE release during the later period.

### 4.1. Methodological considerations

The limitation of this experiment is related to the methodology and the duration of the hind limb ischemia. In a variety of these experimental models for organ ischemia, we chose microsphere injection and iliac artery occlusion for the short and prolonged hind limb ischemia model. A preliminary experiment indicated that common iliac artery occlusion did not yield severe ischemia or muscle necrosis in a chronic ischemic model because collateral flow prevents skeletal muscle ischemia. The combination of artery occlusion and injection of microsphere was used for the hind limb ischemic model. In the hind limb ischemia, however, we did not measure skeletal muscle blood flow. To confirm whether this perturbation induced reduction of blood flow and tissue ischemia, we measured dialysate lactate levels in skeletal muscle as an index of tissue ischemia. This perturbation induced increases in dialysate lactate levels. In the present study, dialysate NE responses were examined in prolonged 6 h ischemia. Temporal changes in MAP and HR appeared but sustained significant hemodynamic changes were not observed. This duration was referred to the experiments on the tourniquet application and release time (Sapega et al., 1985; Mitrev et al., 1996). Four to 6 h of ischemic periods has been thought to produce extensive and reversible damage of skeletal muscle. Therefore, data on pharmacological intervention were obtained within 6 h of skeletal muscle ischemia.

Ischemia induced biphasic NE responses in the skeletal muscle. Initial reduction of NE release may be mediated by an impairment of axonal conduction and/or NE releasing function, while in the later phase, the skeletal muscle ischemia-induced NE release was partly attributable to exocytosis via intracellular $Ca^{2+}$ overload rather than opening of calcium channels or carrier mediated outward transport of NE.

## Acknowledgements

This study was supported by Grants-in Aid for scientific research (15590787) from the Ministry of Education, Culture, Sports, Science and Technology; the Research Grants for Cardiovascular Disease (H13C-1) from the Ministry of Health, Labor and Welfare.

## References

Akiyama, T., Yamazaki, T., Ninomiya, I., 1991. In vivo monitoring of myocardial interstitial norepinephrine by dialysis technique. Am. J. Physiol. 261, H1643–H1647.

Akiyama, T., Yamazaki, T., Ninomiya, I., 1993. Differential regional responses of myocardial interstitial noradrenaline levels to coronary occlusion. Cardiovasc. Res. 27, 817–822.

Akiyama, T., Yamazaki, T., 2001. Myocardial interstitial norepinephrine and dihydroxyphenylglycol levels during ischemia and reperfusion. Cardiovasc. Res. 49, 78–85.

Anton, A.H., Sayer, D.F., 1962. A study of the factors affecting the aluminum oxide-trihydroxyindole procedure for the analysis of catecholamine. J. Pharmacol. Exp. Ther. 138, 360–375.

Barker, D., Saito, M., 1981. Autonomic innervation of receptors and muscle fibers in cat skeletal muscle. Proc. Roy. Soc. Lond., B: Biol. Sci. 212, 317–332.

Cabassi, A., Vinci, S., Quartieri, F., Moschini, L., Borghetti, A., 2001. Norepinephrine uptake is impaired in skeletal muscle of hypertensive rats in vivo. Hypertension 37, 698–702.

Ciuffo, A.A., Ouyang, P., Becker, L.C., Levin, L., Weisfeldt, M.L., 1985. Reduction of sympathetic inotropic response after ischemia in dogs. Contributor to stunned myocardium. J. Clin. Invest. 75, 1504–1509.

Cornett, J.A., Herr, M.D., Gray, K.S., Smith, M.B., Yang, Q.X., Sinoway, L.I., 2000. Ischemic exercise and the muscle metaboreflex. J. Appl. Physiol. 89, 1432–1436.

Cui, J., Wilson, T.E., Shibasaki, M., Hodges, N.A., Grandall, C.G., 2001. Baroreflex modulation of muscle sympathetic nerve activity during postgrip muscle ischemia in human. J. Appl. Physiol. 91, 1679–1686.

Dry, K.L., Phillips, J.H., Dart, A.M., 1991. Catecholamine release from bovine adrenal chromaffin cells during anoxia or metabolic inhibition. Circ. Res. 69, 466–474.

Du, X.-J., Bobik, A., Little, P.J., Esler, M.D., Dart, A.M., 1997. Role of $Ca^{2+}$ in metabolic inhibition-induced norepinephrine release in rat brain synaptosomes. Circ. Res. 80, 179–188.

Fagius, J., Berne, C., 1994. Increase in muscle sympathetic activity in humans after food intake. Clin. Sci. (London) 86, 159–167.

Fern, R., Harrison, P.J., 1994. The relationship between ischaemic conduction failure and conduction velocity in cat myelinated axons. Exp. Physiol. 79, 571–581.

Fujii, T., Kurata, H., Takaoka, M., Muraoka, T., Fujisawa, Y., Shokoji, T., Nishiyama, A., Abe, Y., Matsumura, Y., 2003. The role of renal sympathetic nervous system in the pathogenesis of ischemic acute renal failure. Eur. J. Pharmacol. 481, 241–248.

Hill, J.M., Adreani, C.M., Kaufman, M.P., 1996. Muscle reflex stimulates sympathetic postganglionic efferents innervating triceps surae muscle of cats. Am. J. Physiol. 271, H38–H43.

Idström, J.-P., Soussi, B., Elander, A., Bylund-Fellenius, A.-C., 1990. Purine metabolism after in vivo ischemia and reperfusion in rat skeletal muscle. Am. J. Physiol. 258, H1668–H1673.

Katsuragi, T., Ogawa, S., Furukawa, T., 1994. Contribution of intra- and extracellular $Ca^{2+}$ to noradrenaline exocytosis induced by ouabain and monensin from guinea-pig vas deferens. Br. J. Pharmacol. 113, 795–800.

Kawada, T., Yamazaki, T., Akiyama, T., Sato, T., Shishido, T., Inagaki, M., Tetewaki, T., Yanagiya, Y., Sugimachi, M., Sunagawa, K., 2000. Cyanide intoxication induced exocytotic epinephrine release in rabbit myocardium. J. Auton. Nerv. Syst. 80, 137–141.

Lindsay, T.F., Liauw, S., Romaschin, A.D., Walker, P.M., 1990. The effect of ischemia/reperfusion on adenine nucleotide metabolism and xanthine oxidase production in skeletal muscle. J. Vasc. Surg. 12, 8–15.

Mair, J., 1999. Tissue release of cardiac markers: from physiology to clinical applications. Clin. Chem. Lab. Med. 37, 1077–1084.

Makitie, J., Teravainen, H., 1977. Peripheral nerve injury and recovery after temporary ischemia. Acta Neuropathol. (Berl.) 37, 55–63.

Milusheva, E., Doda, M., Pasztor, E., Lajtha, A., Sershen, H., Vizi, E.S., 1992. Regulatory interactions among axonal terminals affecting the release of different transmitters from rat striatal slices under hypoxic and hypoglycemic conditions. J. Neurochem. 59, 946–952.

Mitrev, Z., Ihnken, K., Poloczek, Y., Hallmann, R., Herold, H., Unkelbach, U., Zimmer, G., Freisleben, H.J., Beyersdorf, S., Beyersdorf, F., 1996. Controlled reperfusion of the extremities for preventing local and systemic damage after prolonged ischemia. An experimental study with the swine model. Zentralbl. Chir. 121, 774–787.

Nukada, H., Dyek, P.J., 1987. Acute ischemia causes axonal stasis, swelling, attenuation and secondary demyelination. Ann. Neurol. 22, 311–318.

Patterson, S., Klenerman, 1979. The effect of pneumatic tourniquets on the ultrastructure of skeletal muscle. J. Bone Joint Surg. Br. 61, 178–183.

Schömig, A., Dart, A.M., Dietz, R., Mayer, E., Kubler, W., 1984. Release of endogenous catecholamines in the ischemic myocardium of the rat. Part A. Locally mediated release. Circ. Res. 55, 689–701.

Schömig, A., Fischer, S., Kurz, T., Richardt, G., Schömig, E., 1987. Non-exocytotic release of endogenous noradrenaline in the ischemic and anoxic rat heart: mechanism and metabolic requirements. Circ. Res. 60, 194–205.

Sapega, A.A., Heppenstall, R.B., Chance, B., Park, Y.S., Sokolow, D., 1985. Optimizing tourniquet application and release times in extremity surgery. A biochemical and ultrastructual study. J. Bone Joint Surg. Am. 67, 303–314.

Tanaka, E., Hattan, N., Ando, K., Ueno, H., Sugio, Y., Mohammed, M.U., Voltchikhina, S.A., Mori, H., 2000. Amelioration of microvascular myocardial ischemia by gene transfer of vascular endothelial growth factor in rabbits. J. Thorac. Cardiovasc. Surg. 120, 720–728.

Thompson, L.P., Mohrman, D.E., 1983. Blood flow and oxygen consumption in skeletal muscle during sympathetic stimulation. Am. J. Physiol. 245, H66–H71.

Tokunaga, N., Yamazaki, T., Akiyama, T., Sano, S., Mori, H., 2003a. In vivo monitoring of norepinephrine and its metabolites in skeletal muscle. Neurochem. Int. 43, 573–580.

Tokunaga, N., Yamazaki, T., Akiyama, T., Sano, S., Mori, H., 2003b. Acute limb ischemia does not facilitate but inhibits norepinephrine release from sympathetic nerve endings in anesthetized rabbit. J. Cardiovasc. Pharmacol. 42, S7–S10.

Toyohara, T., Nada, O., Ikeda, K., 1986. Influence of ischemia on noradrenergic nerves in the terminal colon of humans and rats. Eur. Surg. Res. 18, 349–355.

Turchányi, B., Tóth, B., Rácz, I., Vendégh, Z., Fűrész, J., Hamar, J., 2005. Ischemia reperfusion injury of the skeletal muscle after selective deafferentation. Physiol. Res. 54, 25–31.

Welsh, D.G., Lindinger, M.I., 1993. Energy metabolism and adenine nucleotide degradation in twitch-stimulated rat hindlimb during ischemia-reperfusion. Am. J. Physiol. 264, E655–E661.

Yamada, Y., Teraoka, H., Nakazato, Y., Ohga, A., 1988. Intracellular $Ca^{2+}$ antagonist TMB-8 blocks catecholamine secretion evoked by caffeine and acetylcholine from perfused cat adrenal glands in the absence of extracellular $Ca^{2+}$. Neurosci. Lett. 90, 338–342.

The EMBO Journal (2006) 25, 2889–2897 | © 2006 European Molecular Biology Organization | All Rights Reserved 0261-4189/06
www.embojournal.org

THE EMBO JOURNAL

# Endophilin BAR domain drives membrane curvature by two newly identified structure-based mechanisms

Michitaka Masuda[1,4], Soichi Takeda[2,3,4], Manami Sone[1], Takashi Ohki[1], Hidezo Mori[2], Yuji Kamioka[1] and Naoki Mochizuki[1,*]

[1]Department of Structural Analysis, National Cardiovascular Center Research Institute, Suita, Osaka, Japan, [2]Department of Cardiac Physiology, National Cardiovascular Center Research Institute, Suita, Osaka, Japan and [3]Laboratory of structural biochemistry, RIKEN Harima Institute at SPring-8, Mikazuki-cho, Sayo, Hyogo, Japan

The crescent-shaped BAR (Bin/Amphiphysin/Rvs-homology) domain dimer is a versatile protein module that senses and generates positive membrane curvature. The BAR domain dimer of human endophilin-A1, solved at 3.1 Å, has a unique structure consisting of a pair of helix–loop appendages sprouting out from the crescent. The appendage's short helices form a hydrophobic ridge, which runs across the concave surface at its center. Examining liposome binding and tubulation *in vitro* using purified BAR domain and its mutants indicated that the ridge penetrates into the membrane bilayer and enhances liposome tubulation. BAR domain-expressing cells exhibited marked plasma membrane tubulation *in vivo*. Furthermore, a swinging-arm mutant lost liposome tubulation activity yet retaining liposome binding. These data suggested that the rigid crescent dimer shape is crucial for the tubulation. We here propose that the BAR domain drives membrane curvature by coordinate action of the crescent's scaffold mechanism and the ridge's membrane insertion in addition to membrane binding via amino-terminal amphipathic helix.

*The EMBO Journal* (2006) 25, 2889–2897. doi:10.1038/sj.emboj.7601176; Published online 8 June 2006
*Subject Categories*: membranes & transport; structural biology
*Keywords*: BAR domain; endophilin; liposome; membrane curvature; membrane insertion

## Introduction

Membrane dynamics in a cell, such as membrane budding, tubulation, fission and fusion, is associated with changes in membrane curvature. The crystal structure of amphiphysin BAR (Bin/Amphiphysin/Rvs-homology) domain revealed an unexpected structural identity with arfaptin2, a binding protein to Arf and Rac small GTPases (Tarricone *et al*, 2001), and provided a common structural base for the sensing and the formation of positive curvature membrane by BAR-family proteins (Peter *et al*, 2004).

Endophilins are cytoplasmic proteins containing an N-terminal BAR domain and a C-terminal SH3 domain, and are involved in membrane dynamics (Schuske *et al*, 2003; Galli and Haucke, 2004; Wenk and De Camilli, 2004). There are five endophilin genes in the mammalian genomes, endophilin A1–3 and B1–2. Both A and B types are highly conserved from nematode to human. The most extensively studied one is endophilin-A1, a brain specific protein involved in clathrin-mediated synaptic vesicle endocytosis (Ringstad *et al*, 1997, 2001). Via SH3 domain, endophilins bind to the GTPase dynamin, a membrane scissor, and the polyphosphoinositide phosphatase synaptojanin, a clathrin-uncoater (Ringstad *et al*, 1997; de Heuvel *et al*, 1997; Verstreken *et al*, 2003). The BAR domain of endophilins is classified into the N-BAR subgroup characterized by a short amphipathic helical sequence preceding the consensus BAR-domain sequence (Peter *et al*, 2004). The N-BAR domain of endophilin-A1 binds to liposomes and induces the tubulation *in vitro*, requiring the short amphipathic helical sequence (Farsad *et al*, 2001).

The crescent-shaped BAR dimer structure implies a simple model to drive membrane curvature: the dimer may impress its positively charged concave surface on the negatively charged membrane to form a high-curvature membrane domain (Gallop and McMahon, 2005; McMahon and Gallop, 2005). This curvature-impressing or scaffold mechanism for membrane deformation is based on an assumption that the dimer behaves as a rigid body on the membrane (Zimmerberg and Kozlov, 2006). Although the essential requirement of positively charged residues on the concave surface has been suggested (McMahon and Mills, 2004; Peter *et al*, 2004), there have been no experimental supports for the scaffold mechanism. Here, we show the requirement of the molecular rigidity of the BAR dimer for membrane curvature on the basis of structure-oriented mutational analysis.

By determining the structure of endophilin-A1 BAR domain, we found a distinction from those of the known BAR domains: a helix–loop appendage of 30 amino acids stretch is inserted into the helix 1 of the canonical BAR domain. A pair of the helices of the appendages forms a hydrophobic ridge, which runs across the center of the concave surface of the dimer. We analyzed the function of this ridge as well as the previously proposed structure, the N-terminal amphipathic helix and the crescent main body, for membrane deformation (Peter *et al*, 2004). N-terminal amphipathic helix is essential for membrane binding. The crescent main body of the BAR dimer is required for impressing its intrinsic curvature to the membrane. The ridge contributes to deform the membrane

*Corresponding author. Department of Structural Analysis, National Cardiovascular Center Research Institute, 5-7-1 Fujishiro-dai, Suita, Osaka 565-8565, Japan. Tel.: +81 6 6833 5012; Fax: +81 6 6835 5461; E-mail: nmochizu@ri.ncvc.go.jp
[4]These authors contributed equally to this work

Received: 15 November 2005; accepted: 8 May 2006; published online: 8 June 2006

presumably by penetrating into the membrane. Our results illustrate how these three components coordinate to induce membrane deformation.

## Results

### *Endophilin-A1 BAR domain has a unique appendage*

The structure of the BAR domain of human endophilin-A1 (amino acid 1–247, hereafter EndA1-BAR) was solved at 3.1 Å resolution by a multi-wavelength anomalous dispersion method. The structure of EndA1-BAR dimer is similar to that of amphiphysin (Peter *et al*, 2004) and arfaptin2 (Tarricone *et al*, 2001): a crescent-shaped dimer composed of a 6-helix bundle core and two 3-helix bundle arms extended from the core (Figure 1A). The whole structure of EndA1-BAR dimer can be precisely superimposed on that of amphiphysin and arfaptin (Figure 1B). All three structures show nearly identical dimer shapes. Notably, the present EndA1-BAR structure from a tetragonal crystal packing is almost completely the same as an independent crystal structure from an orthogonal crystal packing (Supplementary Figure 1; and Weissenhorn, 2005). The RMS deviations are 0.63, 0.86 and 0.80 Å for Cα atoms in monomers A, B and dimer, respectively. The structural identity indicates that the crescent shape is stably present in solution. Consistent with previous results (Habermann, 2004; Peter *et al*, 2004), structure-based sequence alignment reveals that these three proteins are poorly conserved in amino-acid sequence including the residues possibly important for the crescent-shape formation (Supplementary Figure 2).

We find a unique structure of the EndA1-BAR, an appendage-like structure protruded from the center of the dimer (Figure 1A). The sequence alignments of the BAR-family proteins indicated that this appendage appears unique to the endophilin-family proteins including nadrin (Habermann, 2004; Peter *et al*, 2004) and the candidates from yeasts (Supplementary Figure 2). The appendage (Q59–Q88) has an N-terminal short helix and a loop of which electron density is mostly missing (N72–G85). The pair of helices appears to stay on the main body and forms a ridge across the center of the concave dimer surface. The helix displays, on its top surface, a series of hydrophobic residues (P62, A63, A66 and M70) aligned 60° against the longitudinal axis of the dimer (Figure 1C). Other than the conserved hydrophobic amino acids of the ridge, the appendage sequences show clear distinction between endophilin-A and endophilin-B (Supplementary Figure 2). The B type endophilins show cytoplasmic localization, presumably being involved in intracellular membrane dynamics (Farsad *et al*, 2001; Modregger *et al*, 2003; Karbowski *et al*, 2004). Analyses of chimeric mutations in the appendage between EndA1-BAR and EndB1-BAR suggest that BAR domain may contribute to defining where to target, plasma membrane or intracellular organ membrane (Supplementary Figure 3).

### *The appendage's penetration enhances liposome tubulation*

To investigate the functional significance of the hydrophobic ridge of the endophilin-specific appendage, we first examined the effects of point mutations in this region (red residues in Figure 1C) on the liposome binding and tubulation activities *in vitro* (Figures 2A and 3). Introduction of membrane-repulsive negative charge (A66D) lost the ability to form tubes from liposomes. Hydrophilic mutations (A63S/A66S (SS) and A63S/A66S/M70Q (SSQ)) reduced the number of tubes (<1/100) and induced three-time enlargement of the tube diameter. In contrast, a bulky hydrophobic residue

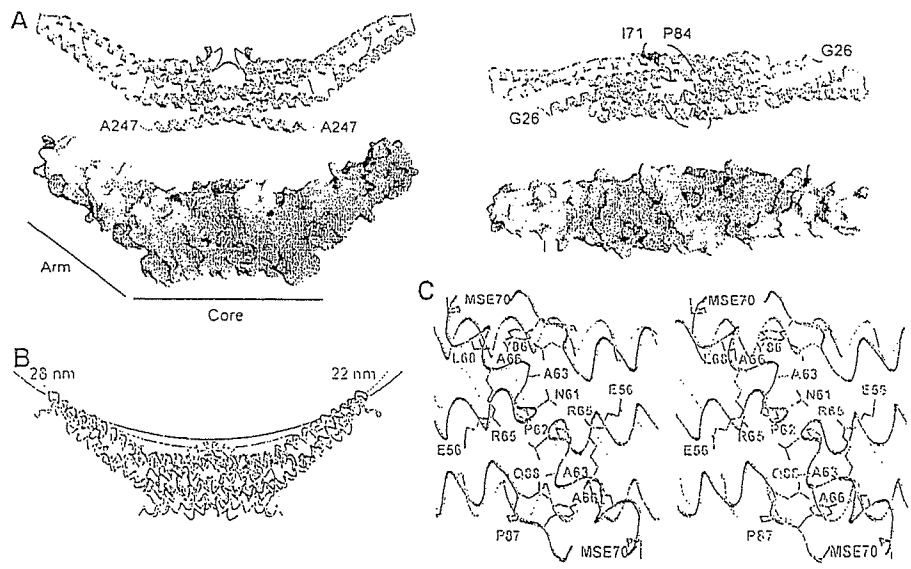


Figure 1 Structure of human endophilin-A1 BAR domain dimer. (A) Ribbon representation (a green monomer with a red appendage and a pale-blue monomer with a blue appendage) and surface electrostatic potential (red, $-15\,kTe^{-1}$; blue, $15\,kTe^{-1}$) of the dimer viewed from the side (left) and from the top (right). The numbered amino-acid residues are the first and the last ones in consecutive polypeptide segments determined in this model. (B) Comparison of three BAR domain structures in trace representation. Red, endophilin-A1 (PDB ID: 1X03); green, amphiphysin (1URU); blue, arfaptin2 (1I4D). The red and green arcs with indicated diameters represent curved membranes fit the concave surface of endophilin-A1 and amphiphysin, respectively. (C) Stereo view of the appendages. Side-chains of the residues forming the hydrophobic ridge and those of interacting with residues of the main body are shown.

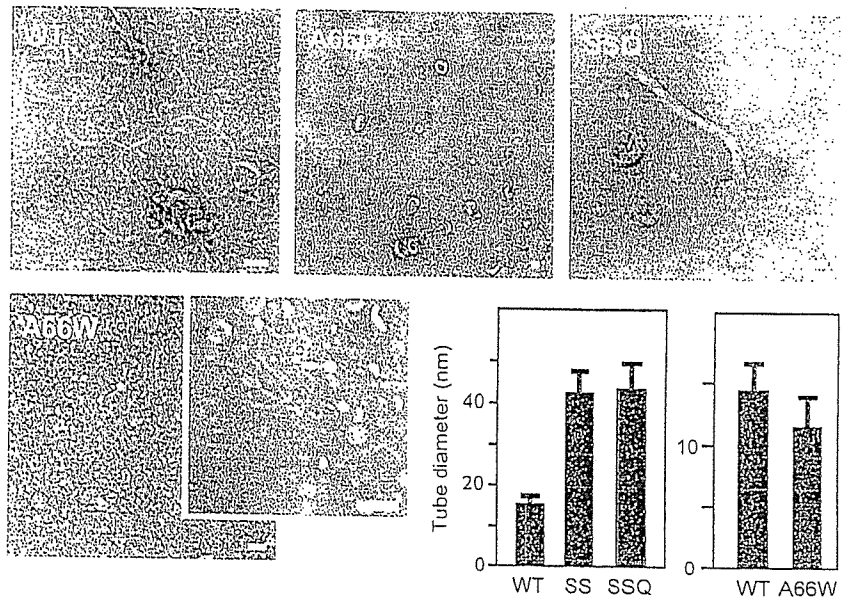


Figure 2 Liposome tubulation by endophilin-A1 BAR domains with mutations in the hydrophobic ridge. WT, 7 μM wild-type BAR domain incubated for 10 min; A66D, 28 μM, 10 min; SSQ, A63S/A66S/M70Q triple mutant, 28 μM, 10 min; A66W, 1.4 μM, 10 min (vesiculated, left panel) and 10 s (tubulated, right panel). Tubulation was not observed when incubated for longer than 1 min. Scale, 100 nm. The bar graphs show tubule diameter (mean and s.d.). SS, A63S/A66S double mutant, 28 μM, 10 min.

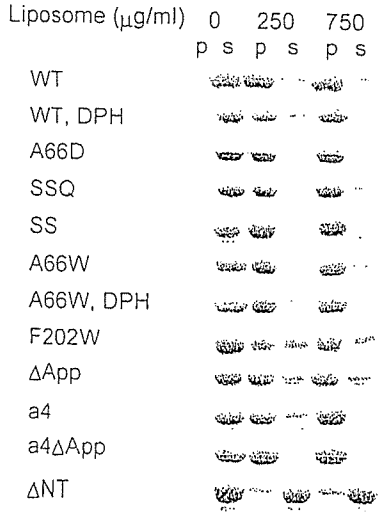


Figure 3 Liposome binding assays of endophilin-A1 BAR domain and its mutants. Protein (200 μg/ml) was co-sedimented with liposomes (0, 250 and 750 μg/ml). Proteins recovered from the pellet (p) and the supernatant (s) were analyzed by SDS–PAGE. The DPH-liposomes show similar binding capacity for the wild type (WT) and the A66W mutants. The liposome binding activity is slightly reduced in the F202W and the appendage-less mutants (ΔApp) and is almost lost in the helix 0 truncated mutant (ΔNT).

(A66W) led to extensive vesiculation and less tubulation. All these mutations did not affect the liposome binding. These results suggest an important role for the hydrophobic ridge in the membrane curvature formation but not in the membrane binding.

Although the ridge reduces the intrinsic curvature of the concave surface (red line in Figure 1B), it appears to promote the membrane curvature formation with conserved hydrophobicity. This raises the possibility that the ridge penetrates into the membrane when the concave surface makes tight contact with the membrane. This possibility was investigated using tryptophan fluorescence, which is sensitive to hydrophobicity of the microenvironment around the indole moiety. The A66W mutant showed 10-nm blueshift of the fluorescence peak in a liposome-dose-dependent and saturable manner, while F202W, a control mutant in which Phe202 on the convex surface was mutated to Trp, did not show any shift (Figure 4A and Supplementary Figure 5). The amount of the blueshift was greater than that observed in 50% DMSO or 50% methanol, indicating that the indol moiety was in a highly hydrophobic environment.

To determine whether this blueshift was caused by the insertion of the indol moiety into the hydrophobic core of the lipid bilayer, we made fluorescence resonance energy transfer (FRET) assays using diphenyl-hexatriene (DPH) as the acceptor probe. DPH has been shown to insert specifically in the nonpolar interior of the membrane and not to alter the membrane structure and dynamics (Repáková *et al*, 2005). DPH liposomes did not affect liposome binding and tubulation (Figure 3 and Supplementary Figure 4). A66W but not F202W showed effective FRET from the 340-nm tryptophan fluorescence (donar) to the DPH fluorescence (acceptor) peaked at 430 nm (Figure 4B and C). It was not caused by changes in the fluorescence property of DPH itself possibly accompanied by tubulation/vesiculation of liposomes (Figure 4D and Supplementary Figure 6). These data suggest that the indol ring of 66W penetrates into the hydrophobic core of the membrane and that the remaining residues of the ridge, about 8 Å in height, appear to be embedded in the layer of lipid head-groups of the contacting membrane leaflet. These results confirmed that the ridge is contacting membrane and that the convex is not contacting membrane surface.

To provide further support for the membrane insertion of the ridge in the wild-type EndA1-BAR, we made a mutant

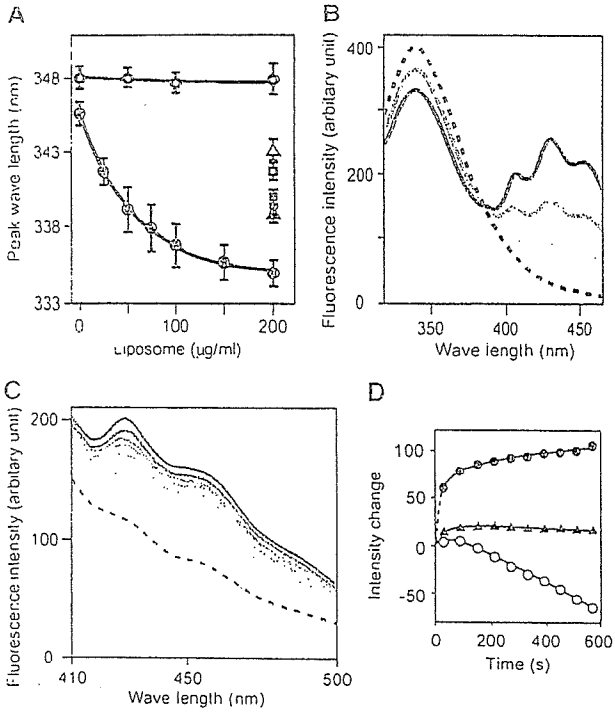


Figure 4 Tryptophan fluorescence blueshift and FRET assays. (A) Tryptophan fluorescence emission peak when excited at 280 nm was observed in different concentration of liposome. A66W (●), F202W control mutant (○), A66W alone in 50% DMSO (▲), in 50% MeOH (■), F202W alone in 50% DMSO (△), in 50% MeOH (□), 140 μg/ml protein for all measurements. Mean and s.d. ($N = 4$–11). The dose dependency is significant ($P \ll 0.001$) for the A66W mutant but insignificant ($P > 0.8$) for the F202W mutant (one-way ANOVA). DMSO and MeOH were used as blueshift inducer for tryptophan. (B) Dose-dependent FRET efficiency from the A66W tryptophan to DPH incorporated in liposomes was examined by the changes of fluorescence. Fluorescence spectrum of A66W (100 μg/ml) with the control liposome (200 μg/ml) excited at 280 nm (hatched). Pale to dark solid curves represent DPH:lipid weight ratios of 1:2000, 1:1000 and 1:500 in the same condition. (C) Time-dependent increase in the FRET efficiency from either A66W (pale to dark solid lines, from 30 to 570 s) or F202W tryptophan (pale and dark hatched lines, at 30 and 570 s) to DPH incorporated in liposomes. DPH:lipid weight ratio is 1:500. (D) The intensity changes at the 430-nm peak are plotted against time. A66W (●), F202W (▲) excited at 280 nm and A66W (○) excited at 360 nm.

with amphiphysin/arfaptin shape and examined its tubulation activity. The mutant (ΔApp), in which the entire appendage (Q59–Q88) was replaced with a helical stretch (AHLSSLLQ) derived from arfaptin2 sequence (A152–Q159, Y155S), show the crystal structure of a canonical BAR-domain dimer as designed (Figure 5A and Supplementary Figure 7). The ΔApp could bind to liposomes (Figure 3) and cause tubulation to a lesser extent than the wild type and amphiphysin-BAR (Figure 5D and Supplementary Figure 4). As the diameter of the tubules reflects the membrane curvature if the section of the tube is circle, we measured the diameter of the tube to compare the curvature of the EndA1-BAR and its mutant-induced tubes. Despite the higher curvature of the concave surface, the ΔApp dimer induced larger diameter tubules than the wild type did, indicating a positive contribution of the wild-type hydrophobic ridge to drive membrane curvature. Taken all together, the hydrophobic ridge penetrates into the interfacial leaflet of the lipid bilayer when the concave surface is in contact with the membrane and promotes membrane curvature formation.

### *The BAR domain is rigid enough to impose its intrinsic curvature on membrane*

A simple model for the concave surface-driven mechanism is that each BAR domain dimer acts as a molecular mold that impresses its curved surface on the membrane. This model suggests that the membrane curvature approximately mirrors the curvature of the concave surface. Indeed, the diameters of tubules induced by amphiphysin, ΔApp (Figure 5D), SS and SSQ mutants (Figure 2) are compatible with the model-based prediction (see Supplementary Table II for statistical analysis). However, this model has an assumption that the dimer should be rigid enough to overcome the bending resistance of the membrane (Nossal and Zimmerberg, 2002; Farsad and De Camilli, 2003). To examine whether the molecular mold mechanism is feasible, we developed a straight BAR domain by inserting one helical pitch into the helix II in the proximal portion of the extending arm (QSAL is inserted between I154 and Q155). This mutation (a4) would compensate the unequal lengths between helix II and III in the arm, a common feature of the known BAR domain structures, and let the curved arm into a straight one. Although the a4 mutant was designed simply to straighten the curvature of the domain, the structure solved at 2.4 Å resolution shows that it actually has the very interesting property of a flexible arm rather than a rigid one (Figure 5B). Four monomers in the asymmetrical unit show deviation in the bending angles of arms. The blue and the green monomers have straight arms while the orange monomer shows a bending pattern similar to the wild type and the yellow monomer is an intermediate. The structural deviation almost exclusively occurs in the helix kink regions (Supplementary Figure 8), indicating that the arm can swing at least from the bend-free straight position to nearly the wild-type position.

The a4 mutant allowed us to examine how flexibility of the crescent-shaped main body of the BAR dimer affects the membrane curvature formation. The insertion of one helical pitch slightly distorts relative position of the helix II and III (Figure 5C), but does not largely rearrange the spatial positions of the residues on the concave surface of the arm (Supplementary Figure 8). Indeed, the a4 mutant and its appendage-lacking derivative (a4ΔApp) retained normal liposome binding activity (Figure 3). The a4 mutant vesiculated liposomes without any tubulation, while a4ΔApp lost these membrane-deforming activities (Figure 5D and Supplementary Figure 4). The concave surface-induced membrane deforming activity appeared to be lost in the a4 mutant, while the appendage's membrane insertion remained active. These results suggested that the rigidity of the crescent dimer structure is essential for liposome tubulation but not for vesiculation, although appendage insertion induces the vesiclulation.

### *Roles for the amphipathic helix 0 of the N-BAR domain*

The structure of a short amphipathic helix (helix 0) characterizing the N-BAR (Peter *et al*, 2004) can be resolved in the a4 mutant structure due to its tight crystal packing (Figures 5B and 6). The helix 0 is disordered in the wild type (Figure 6) and the ΔApp structures. The helix 0 has been

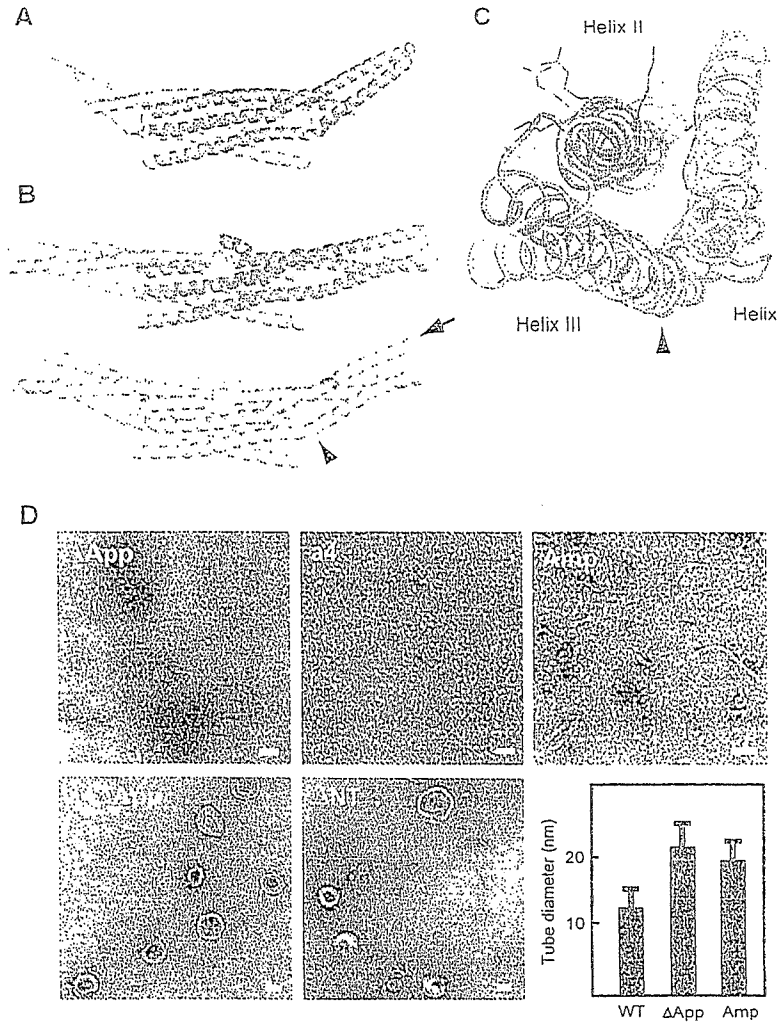


Figure 5 Distinct liposome tubulation induced by endophilin-A1 BAR domain mutants. (A) Ribbon representation of a mutated EndA1-BAR dimer lacking the entire appendages (ΔApp, PDB ID: 1X04). The entire appendage (Q59–Q88) was replaced with a helical stretch (AHLSSLLQ) derived from arfaptin2 sequence (A152–Q159, Y155S). Red, mutated segment. (B) Ribbon representation of the a4 mutant with swinging arms (PDB ID: 2D4C). One helical pitch was inserted into the helix II in the proximal portion of the extending arm (QSAL was inserted between I154 and Q155). Two dimers in the asymmetrical unit are shown separately. Red, inserted segment; magenta, helix 0. The bending patterns of the helix II and III varies among four monomers. An obvious kink in the helix III remains in the orange monomer (arrowhead, also in (C)). The residual curvature in the blue–green dimer is provided by the intersection of the monomers. (C) Superimposition of the a4 mutant monomer (orange one in (B)) and the wild-type monomer (blue) in the core region. A view from the distal end along the helix II (arrow in (B)) shows the maximum structural difference in these arms. Side chains of K171, 173 and R174 are shown. The helix III rotates 12° counterclockwise and shift 6 Å relative to the helix II at the distal end of the arm. The helix 0 and the core region are omitted. (D) Negatively stained liposome tubules induced by the BAR domains of endophilin mutants and amphiphysin. ΔApp, 7 μM, incubated for 10 min; a4, 7 μM, 10 min; a4ΔApp, 28 μM, 10 min; ΔNT, 21 μM, 10 min; Amp, 7 μM, 10 min. Note that a4, a4ΔApp, and ΔNT do not induce liposome tubulation. Scale, 100 nm. The bar graph shows tubule diameter (mean and s.d.).

suggested to be helical only when the amphiphysin BAR domain binds to liposomes (Peter *et al*, 2004). The helix 0 displays the hydrophobic branch of T14, V17 and V21 on one side, while K12, K16 and E19 on the other side (Figure 6). The helix 0 is connecting with the Helix I by a flexible linker G23–G24–A25. Consistent with the previous report (Farsad *et al*, 2001), truncation of the helix 0 (ΔNT) resulted in loss of liposome binding activity (Figure 3) and consequently abolished the tubulation (Figure 5D). In contrast, all the helix 0-containing mutants, including the A66D and the a4ΔApp showed intact liposome binding activity irrespective of their tubulation or vesiculation activities. These results indicate that the helix 0 in the endA1-BAR is critical for liposome binding and that the membrane binding of endA1-BAR via helix 0 is not sufficient to induce tubulation or vesiculation.

### *BAR domain induces tubular membrane deformation in vivo*

To explore the significance of the helix 0, the rigid crescent mold, and the appendage of endophilin-A1 BAR domain *in vivo*, we further examined the membrane deformation activity of endophilin-A1 BAR domain in cells (Figure 7). Human umbirical vascular endothelial cells (HUVECs) expressing endophilin-A1 lacking SH3 domain (residues 1–296, hereafter, EndA1-BAR296), which was C-terminally tagged with enhanced green fluorescence protein (EGFP), exhibited intracellular fibrous structure similar to those induced by other BAR domain-containing molecules (Kamioka *et al*, 2004; Itoh *et al*, 2005). Notably, these structures developed from the periphery toward the center of the cells dynamically and disappeared reversibly in living cells (Figure 7E and

Supplementary Movie 1). Furthermore, these GFP-marked structures were co-localized with *in vivo* biotin-labeled membrane (Figure 7D), indicating that EndA1-BAR296-induced fibrous structure seems to be a membrane invagination originated from the plasma membrane. These structures were found in other cells we tested (Figure 7C). In clear contrast, ΔApp, ΔNT and a4 were incapable of inducing membrane deformation in cells, indicating the importance of helix 0, the rigid crescent shape, and the appendage of BAR domain for membrane deformation *in vivo*.

## Discussion

The endophilin-A1 BAR domain dimer consists of three sub-modules: the crescent-shaped main body, the helix 0 and the unique appendage. We tried to understand the functional roles for these sub-modules in the membrane curvature formation. In this study by determining the structure of endopholin-A1 BAR domain and developing mutants that were critical for the sub-module structure, we have explored the roles of sub-modules.

Here, we show that the structural rigidity of the crescent-shaped main body is critical for membrane tubulation. The BAR dimer is sufficiently rigid to overcome the bending resistance of the membrane and to be scaffolds for the tubulation (McMahon and Gallop, 2005; Zimmerberg and Kozlov, 2006). The insertion of one helical-pitch into the helix II at distal to the kink brings flexibility to the dimer (a4 mutant). The relative position of the three helices in the

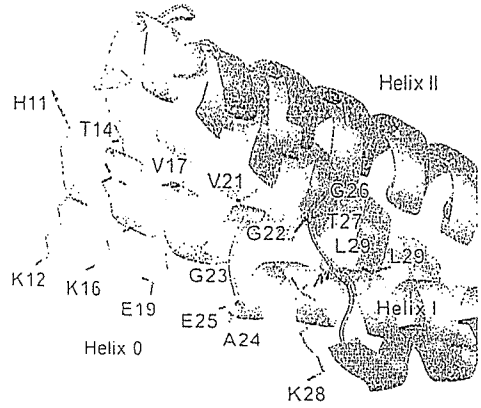


Figure 6 Close-up of helix 0 in an a4 mutant monomer (orange). The same superimposition as in Figure 5C but viewed from the side and displays the helix 0. The helix 0 is disordered in the wild-type structure (blue). The side chains of N-terminal residues are shown (H11KATQKVSEKVGGAEGTKL29 in the a4 and G26TKL in the wild type). The amphipathic helix 0 is stabilized by hydrophobic interactions with the helix II and III and also by hydrogen bonds with a symmetrical molecule.

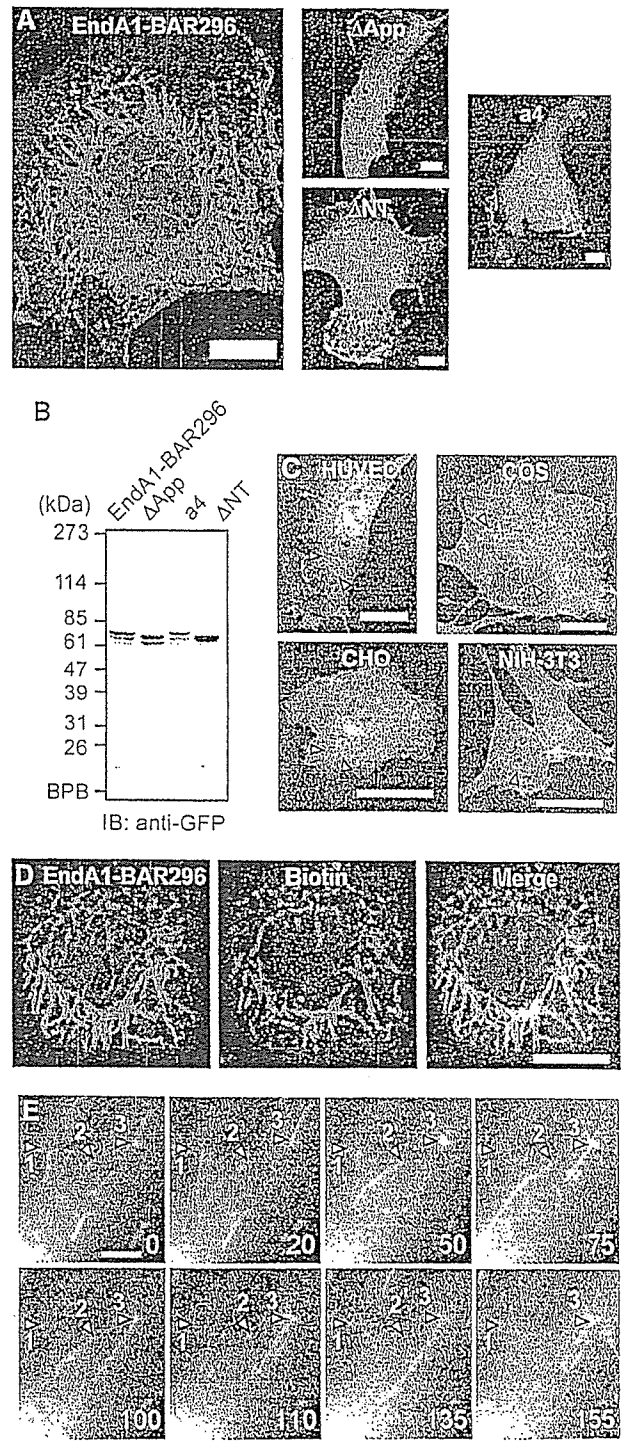


Figure 7 Endophilin A1 BAR domain induces membrane tubulation *in vivo*. (A) HUVECs were transfected with plasmids expressing C-teminally EGFP-tagged EndA1-BAR296 (amino acid 1–296 of endophilin-A1), ΔApp, a4, and ΔNT. Cells were GFP-imaged on an epifluorescnce microscope (Olympus IX-71). Fibrous structures were observed exclusively in EndA1-BAR296-expressing cells. Scale, 10 μm. (B) Protein expression of the EndA1-BAR296 and the mutants tagged with EGFP in transfected 293T cells were examined by immunoblotted with anti-GFP antibody. (C) Cells indicated were similarly transfected to (A). Arrowheads indicate the fibrous structures. Scale, 20 μm. (D) Live HUVECs expressing EGFP-tagged EndA1-BAR296 were biotinylated with sulfo-NHS-biotin for 10 min and chased for further 10 min. Covalently bound biotin was visualized using Alexa633-streptavidine. Fluorescnece images for EGFP (left), Alexa633 (center), and merge (right) are shown. Scale, 10 μm. (E) A time lapse images of HUVECs expressing EGFP-tagged EndA1-BAR296 were obtained at the time point (seconds) after the observation (Supplementary Movie 1). EGFP-marked structure grows from the cell periphery towards the center of the cell. Notably, both extension and retraction of GFP-marked structure is observed (numbered arrow heads indicate each extending/retracting structure). Scale, 5 μm.

mutant arm was not changed in a4 mutant irrespective of the bend levels (Supplementary Figure 8). The mutant arm behaves as a rigid body and its structure changes only in the vicinity of the helix kinks when it swings. Therefore, it is unlikely that the flexibility of the mutant dimer can be a result of weakened inter-helix interactions in the arm. Moreover, we could not find any specific structural features in the kink region that might explain the flexible hinge in the swinging-arm mutant as well as the rigid bend in the wild-type BAR dimers of endophilin, amphiphysin, and arfaptin.

In this study, for the first time we could determine the structure of the N-terminal amphipathic helix (helix 0) using a swinging-arm mutant. Our mutant and previous mutation analyses indicated that the N-terminal helical sequence of endophilin-A1 is indispensable for liposome binding (Farsad *et al*, 2001), whereas that of amphiphysin is important but not essential for liposome binding and tubulation (Peter *et al*, 2004). The BAR domain of endophilin-A1 is an acidic polypeptide and the cluster of positive charge at the distal end of the arm is not prominent (Figure 1A). This property can explain the critical role for the helix 0 of the EndA1-BAR in liposome binding by providing additional basic residues. The helix 0 structure suggests that K12, K16 and possibly K8 are in a suitable position for cooperation with the positive charge cluster at the distal end. The amphipathic nature of the helix 0 implies that it can also insert into the membrane and facilitate the membrane curvature formation (Peter *et al*, 2004; Gallop and McMahon, 2005; McMahon and Gallop, 2005). Loss of the membrane-deforming activities of the A66D mutant (Figure 2) and the a4ΔApp mutant (Figure 5D) accounts for the additional mechanism for membrane deformation in addition to the membrane insertion of the helix 0.

The N-BAR of endophilins has one additional step to tubulate membrane. Here, we show that the hydrophobic ridge of the endophilin-specific appendage is inserted into the contacting membrane surface. Our data suggested that the entire ridge of the wild-type BAR domain, about 8 Å in height, is embedded in the layer of lipid head-groups of the contacting membrane leaflet. The embedding of the ridge into the membrane is consistent with the local spontaneous curvature mechanism that is reported very recently (Zimmerberg and Kozlov, 2006). As a protruding structure found in epsin1 induces liposome tubulation by being inserted to one leaflet of the lipid bilayer (Ford *et al*, 2002), the penetration of the hydrophobic ridge can drive the positive curvature by causing asymmetrical expansion of the surface area between two leaflets as shown in Figure 8 (Farsad and De Camilli, 2003).

We further explored the importance of the ridge, rigid crescent shape, and helix 0 in cells. We for the first time showed that N-BAR domain induced membrane invaginations originated from plasma membrane, although other BAR-containing molecules have been reported to induce similar invaginations (Itoh *et al*, 2005). Neither mutant that lacked either the ridge or the helix 0 nor flexible mutant formed the tubular invaginations in cells, indicating the significance of these sub-module structure in cells as suggest by *in vitro* studies. We constructed a series of endorphin-A1-EGFP expression plasmids to delineate the domain for the membrane invagination. Full-length endophilin-expressing cells did not show any tubular formation. Because endophilin consists of BAR domain and an SH domain, SH3-binding molecule such as dynamin may inhibit the extension of membrane invagination. This possibility has been suggested in the membrane invagination found in FBP17 and amphiphysin (Kamioka *et al*, 2004; Itoh *et al*, 2005).

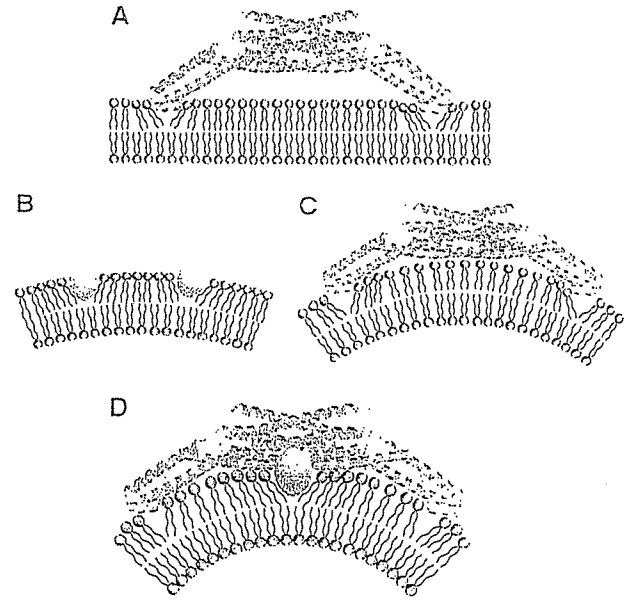


Figure 8 Two potential mechanisms for driving membrane curvature by endophilin-A1. (A) Kissing adhesion of an N-BAR domain on planar lipid bilayer. The helix 0 is essential for the membrane binding. Membrane insertion of the helix 0 is supposed. (B) Insertion of hydrophobic portions of macromolocules into one leaflet can create bilayer surface discrepancy that causes membrane curvature. (C) The simple N-BAR domain, such as amphiphysin and ΔApp, induces membrane curvature by impressing the concave surface onto the membrane. The rigidity of the molecule is required for this mechanism. (D) To drive membrane curvature, the endophilin N-BAR domain uses both the rigid crescent shape-mediated deformation and the insertion of hydrophobic ridge on the concave surface in addition to kissing adhesion of N-BAR to membrane surface.

Collectively, EndA1-BAR uses two newly identified mechanisms to drive positive membrane curvature in addition to the essential binding capacity of helix 0 to the membrane: one by the scaffold mechanism common to the BAR domains and the other by the local spontaneous curvature mechanism caused by the membrane insertion of the ridge (Figure 8D). The ridge, which occupies the bottom of the concave lipid-binding surface, may not work until the main body of the BAR dimer localizes itself to a curved membrane. The ridge then inserts into the bilayer roughly perpendicular to the main body, and thus both deformations will occur in the same direction.

## Materials and methods

### *Protein expression and purification by CRECLE*

cDNAs encoding BAR domains (amphiphysin1, 1–239; endophilin-A1, 1–247; endophilin-B1, 1–246 in amino-acid residues) were amplified by PCR from a human brain cDNA library. Recombinant proteins were expressed in *Escherichia coli* as GST-fusions using the pGEX6p3 vector, purified by glutathione-Sepharose, cleaved from the GST-tag using Prescission protease (Amersham Biosciences), and further purified by ion-exchange chromatography (Yamagishi *et al*, 2004). The final polypeptide contained an artificial linker

sequence of GPLGS at the N-terminus. EndA1-BAR proteins except for F202W and a4 mutants were purified by crystallization during Prescission protease cleavage. The method, crystallization by regulated cleavage of large hydrophilic tag (CRECLE), was as follows. Purified GST fusions were concentrated to 20–30 mg/ml in an elution buffer (20 mM glutathione, 100 mM Tris-HCl, pH 8.0, 10 mM DTT, 1 mM EDTA, 1 mM EGTA) and then cleaved by a low concentration of prescission protease (1 U/mg protein or less) at 4°C. Slow increase in the tag-free protein concentration might be suitable for crystallization and more than a half of EndA1-BAR protein could be recovered as 20–100 μm microcrystals. They were washed with a low-salt buffer (20 mM HEPES, pH 7.4, 2 mM DTT, 0.2 mM EDTA, 0.2 mM EDTA) and resolved into a high-salt buffer (350 mM NaCl in the low-salt buffer) and used for further analyses.

### *Protein crystallization*

Seleno-methionine (S-Met) derivatives of the EndA1-BAR domain and its appendage-less mutant (ΔApp) were produced in B834(DE3)pLysS cells using Overnight Express Autoinduction System 2 (Novagen). To make X-ray grade crystals in a cryo-ready condition, modified high salt buffer (50 mM HEPES, pH 7.4, 300 mM NaCl, 100 mM KI, 28% ethylene glycol, 5% glycerol, 25 mM DTT) was used. Crystals of 1 mm size were formed by dialysis against 50 mM CHES, pH 9.5, 260 mM NaCl, 28% ethylene glycol, 5% glycerol, 25 mM DTT, 0.4% benzamidine·HCl at 4°C and were flush frozen at 100 K. Crystals could also be grown by vapor diffusion from a similar protein solution using distilled water as the bath solution. The crystals were equilibrated in 50 mM HEPES, pH 7.4, 150 mM NaCl, 25 mM DTT, 0.4% benzamidine·HCl, 5% PEG 8000 and the saturated amount of xylitol as a cryoprotectant. Some of the crystals were soaked with 0.5 mM oleoyl-L-α-lysophosphatidic acid (Sigma) or malonyl-CoA (Sigma) for 4 days with daily change for the substrates. The a4 mutant crystals were grown by sitting-drop vapour diffusion using a bath solution containing 100 mM HEPES, pH 7.2, 200 mM calcium acetate, 10 mM DTT and 20% (w/v) PEG3350 at 20°C and then flush frozen after brief immersion in the same solution containing 16% DMSO. The wild type and the ΔApp mutant crystals belong to the same space group $I4_1$ and contain one monomer molecule in the asymmetric unit (Supplemental Figure 1). The a4 crystal belongs to $P2_1$ and contains two dimers in the asymmetric unit.

### *Structural determination*

The EndA1-BAR structure was determined using the multiple anomalous dispersion (MAD) method. Multiple-wavelength X-ray diffraction data sets were collected from a single Se-Met crystal (crystal I) at SPring-8 beamline BL44B2 (Supplementary Table I). Single wavelength data sets of another crystal (crystal II) and of a ΔApp crystal used for the refinement were collected at BL45PX. The data set for the a4 mutant was collected at BL38B1. All diffraction data sets were collected at 90 K and were processed using HKL2000 suite (Otwinowski and Minor, 1997). The seven positions out of 10 expected selenium atoms were identified by SOLVE (Terwilliger and Berendzen, 1999). The initial phases calculated by SOLVE with a figure of merit of 0.59 at 3.2 Å resolution were further improved by RESOLVE (Terwilliger, 1999). The density modified MAD map (Supplementary Figure 1) had sufficient quality to trace the polypeptide chain except for the N-terminus and the loop region of the appendage. The model was built with TURBO-FRODO (Roussel and Cambillau, 1996) and refined to the resolutions of 3.1 Å by CNS (Brunger *et al*, 1998). The final model includes 210 residues (residues 26–71 and 84–247), and has an $R$ factor of 23.6% ($R_{free}$ of 26.4%). The ΔApp structure was solved by molecular replacement by MOLREP in the CCP4 suite (CCP4, 1994) and refined to the resolution of 2.9 Å by CNS. The simulated annealing omit electron density map calculated by CNS confirmed the continuous α-helical structure of the replaced region as designed (Supplementary Figure 7). The final model includes 200 amino-acid residues and has an $R$ factor of 23.8% ($R_{free}$ of 26.9%). The a4 mutant structure was solved by molecular replacement using the central core of the EndA1-BAR as a starting model and the arms were manually built (Supplementary Figure 7). The structure was refined to the resolution of 2.4 Å by CNS with an $R$ factor of 21.5% ($R_{free}$ of 26.9%). Main-chain dihedral angles of all non-glycine residues of these three models lie in allowed regions of the Ramachandran plot, with 94.3% for the EndA1-BAR, 94.1% for the ΔApp mutant, and 96.4% for the a4 mutant in most-favored regions, respectively. Graphical representations were prepared using the programs TURBO-FRODO, MOLSCRIPT (Kraulis, 1991), RASTER3D (Merritt and Bacon, 1997), GRASP (Nicholls *et al*, 1991) and Pymol (DeLano, 2002).

### *Liposome binding and tubulation assays*

Liposome sedimentation assay and tubulation assay were as earlier described (Peter *et al*, 2004 see also McMahon lab protocols: http://www2.mrc-lmb.cam.ac.uk/NB/McMahon_H/group/techniqs/techniqs.htm) with slight modifications. Briefly, Folch fraction 1 (Sigma) was used as the lipid source and liposome suspension, 1 mg/ml in liposome buffer (20 mM HEPES, pH 7.4, 150 mM NaCl, 1 mM DTT) was made by sonication. Freshly purified BAR domain proteins were diluted at about 1 mg/ml in the liposome buffer and ultracentrifuged at 400 000 *g* for 10 min just before use. No crystallization occurred at this or lower concentrations. For sedimentation assays, 20 μg proteins were mixed with 25 or 75 μg liposomes in 100 μl of the liposome buffer, incubated for 10 min on ice and ultracentrifuged at 200 000 *g* for 10 min. For tubulation assays, 400 μg/ml proteins were mixed with an equal volume of 400 μg/ml liposomes, left for 10 s to 30 min at room temperature, and then processed for negative staining. Judging from the liposome sedimentation and the tryptophan fluorescence assays, this protein to lipid ratio ensured nearly saturated protein–liposome binding. Magnification was calibrated using a grating replica of 2160/mm.

### *Tryptophan fluorescence and FRET assay*

Fluorescence emission spectra were recorded with a Hitachi F-4500 fluorescence spectrophotometer (Ohki *et al*, 2004). For tryptophan fluorescence assays, 140 μg/ml tryptophan-containing mutants were mixed with 0–200 μg/ml liposomes in the liposome buffer, incubated for 3 min, and excited at 280 nm. For FRET assays, DPH-liposomes were made by adding DPH (Molecular Probe) into lipid solution (1:500 to lipid, w:w). The fluorescence of DPH-liposomes (200 μg/ml) excited at 280 nm was scanned from 400 to 500 nm at 1-min intervals. The first measurement of the 430-nm DPH peak was obtained at about 30 s after mixing with mutant proteins (100 μg/ml).

### *Cell culture, transfection and surface biotinylation*

HUVECs were purchased from Kurabo and cultured in HuMedia-EG2 as described previously (Sakurai *et al*., 2006). 293T cells, CHO cells, Cos7 cells, and NIH-3T3 cells were cultured in DMEM supplemented with 10% fetal bovine serum as described previously (Kamioka *et al*., 2004). Cells were transfected using LipofectAMINE 2000 (Invitrogen). Live HUVECs were biotinylated with 5 mM sulfo-NHS-biotin (Pierce) in Opti-MEM (Invitrogen) for 10 min. They were washed once with Opti-MEM and chased for 10 min with the normal culture medium, and fixed with 2% formaldehyde after a brief wash with Opti-MEM containing 1/20 volume of Avidin D blocking solution (Vector Laboratory) to reduce the cell surface background staining. HUVECs were permeabilized with cold MeOH and biotin was visualized using Alexa633-streptavidine (Molecular Probe).

### *Supplementary data*

Supplementary data are available at *The EMBO Journal* Online.

## Acknowledgements

We thank H Nakajima, T Matsu, Y Kawano and H Naitow for technical assistance with SPring-8 beamlines, and H Ago and M Miyano, Structural Biophysics Laboratory, RIKEN Harima Institute at SPring-8, for their helpful advice. This work was supported in part by Grant for Research on Advanced Medical Technology from the Ministry of Health, Labour, and Welfare of Japan, by the Program for Promotion of Fundamental Studies in Health Sciences of the National Institute of Biomedical Innovation (NIBIO), and by Special Coordination Funds for Promoting Science and Technology, Ministry of Education, Culture, Sports, Science and Technology (MEXT) of Japan.

Competing interests statement

The authors declare that they have no competing commercial interests in relation to this work.

## References


Brunger AT, Adams PD, Clore GM, DeLano WL, Gros P, Grosse-Kunstleve RW, Jiang JS, Kuszewski J, Nilges M, Pannu NS, Read RJ, Rice LM, Simonson T, Warren GL (1998) Crystallography & NMR system: a new software suite for macromolecular structure determination. *Acta Crystallogr D* 54: 905–921

Collaborative Computational Project Number 4 (1994) The CCP4 suite: programs for protein crystallography. *Acta Crystallogr D* 50: 760–763

DeLano WL (2002) *The PyMOL User's Manual*. DeLano Scientific: San Carlos, CA, USA

Galli T, Haucke V (2004) Cycling of synaptic vesicles: How far? How fast!. *Sci STKE* 2004: re19

Farsad K, Ringstad N, Takei K, Floyd SR, Rose K, De Camilli P (2001) Generation of high curvature membranes mediated by direct endophilin bilayer interactions. *J Cell Biol* 155: 193–200

Farsad K, De Camilli P (2003) Mechanisms of membrane deformation. *Curr Opin Cell Biol* 15: 372–381

Ford MG, Mills IG, Peter BJ, Vallis Y, Praefcke GJ, Evans PR, McMahon HT (2002) Curvature of clathrin-coated pits driven by epsin. *Nature* 419: 361–366

Gallop JL, McMahon HT (2005) BAR domains and membrane curvature: bringing your curves to the BAR. *Biochem Soc Symp* 72: 223–231

Habermann B. (2004) The BAR-domain family of proteins: a case of bending and binding. *EMBO Rep* 5: 250–255

de Heuvel E, Bell AW, Ramjaun AR, Wong K, Sossin WS, McPherson PS (1997) Identification of the major synaptojanin-binding proteins in brain. *J Biol Chem* 272: 8710–8716

Itoh T, Erdmann KS, Roux A, Habermann B, Werner H, De Camilli P (2005) Dynamin and the actin cytoskeleton cooperatively regulate plasma membrane invagination by BAR and F-BAR proteins. *Dev Cell* 9: 791–804

Kamioka Y, Fukuhara S, Sawa H, Nagashima K, Masuda M, Matsuda M, Mochizuki N. (2004) A novel dynamin-associating molecule, formin-binding protein 17, induces tubular membrane invaginations and participates in endocytosis. *J Biol Chem* 279: 40091–40099

Karbowski M, Jeong SY, Youle RJ (2004) Endophilin B1 is required for the maintenance of mitochondrial morphology. *J Cell Biol* 166: 1027–1039

Kraulis PJ (1991) MOLSCRIPT: a program to produce both detailed and schematic plots of protein structure. *J Appl Crystallogr* 24: 946–950

McMahon HT, Mills IG (2004) COP and clathrin-coated vesicle budding: different pathways, common approaches. *Curr Opin Cell Biol* 16: 379–391

McMahon HT, Gallop JL (2005) Membrane curvature and mechanisms of dynamic cell membrane remodeling. *Nature* 438: 590–596

Merritt EA, Bacon DJ (1997) Raster3D: photorealistic molecular graphics. *Methods Enzymol* 277: 505–524

Modregger J, Schmidt AA, Ritter B, Huttner WB, Plomann M (2003) Characterization of Endophilin B1b, a brain-specific membrane-associated lysophosphatidic acid acyl transferase with properties distinct from endophilin A1. *J Biol Chem* 278: 4160–4167

Nicholls A, Sharp K, Honig B (1991) Protein folding and association: insights from the interfacial and thermodynamic properties of hydrocarbons. *Proteins* 11: 281–296

Nossal R, Zimmerberg J (2002) Endocytosis: curvature to the ENTH degree. *Curr Biol* 12: R770–R772

Ohki T, Mikhailenko SV, Morales MF, Onishi H, Mochizuki N (2004) Transmission of force and displacement within the myosin molecule. *Biochemistry* 43: 13707–13714

Otwinowski Z, Minor W (1997) Processing of X-ray diffraction data collected in oscillation mode. *Methods Enzymol* 276: 307–326

Peter BJ, Kent HM, Mills IG, Vallis Y, Butler PJ, Evans PR, McMahon HT (2004) BAR domains as sensors of membrane curvature: the amphiphysin BAR structure. *Science* 303: 495–499

Repáková J, Holopainen JM, Morrow MR, McDonald MC, Capkova P, Vattulainen I (2005) Influence of DPH on the structure and dynamics of a DPPC bilayer. *Biophys J* 88: 3398–3410

Ringstad N, Nemoto Y, De Camilli P (1997) The SH3p4/Sh3p8/SH3p13 protein family: binding partners for synaptojanin and dynamin via a Grb2-like Src homology 3 domain. *Proc Natl Acad Sci USA* 94: 8569–8574

Ringstad N, Nemoto Y, De Camilli P (2001) Differential expression of endophilin 1 and 2 dimers at central nervous system synapses. *J Biol Chem* 276: 40424–40430

Roussel A, Cambillau C (1996) *TURBO-FRODO Manual*. Marseille France AFMB-CNRS, Paris, France

Sakurai A, Fukuhara S, Yamagishi A, Sako K, Kamioka Y, Masuda M, Nakaoka Y, Mochizuki N (2006) MAGI-1 is required for Rap1 activation upon cell–cell contact and for enhancement of vascular endothelial cadherin-mediated cell adhesion. *Mol Biol Cell* 17: 966–976

Schuske KR, Richmond JE, Matthies DS, Davis WS, Runz S, Rube DA, van der Bliek AM, Jorgensen EM (2003) Endophilin is required for synaptic vesicle endocytosis by localizing synaptojanin. *Neuron* 40: 749–762

Tarricone C, Xiao B, Justin N, Walker PA, Rittinger K, Gamblin SJ, Smerdon SJ (2001) The structural basis of Arfaptin-mediated cross-talk between Rac and Arf signalling pathways. *Nature* 411: 215–219

Terwilliger TC (1999) Reciprocal-space solvent flattening. *Acta Crystallogr D* 55: 1863–1871

Terwilliger TC, Berendzen J (1999) Automated MAD and MIR structure solution. *Acta Crystallogr D* 55: 849–861

Verstreken P, Koh TW, Schulze KL, Zhai RG, Hiesinger PR, Zhou Y, Mehta SQ, Cao Y, Roos J, Bellen HJ (2003) Synaptojanin is recruited by endophilin to promote synaptic vesicle uncoating. *Neuron* 40: 733–748

Weissenhorn W (2005) Crystal structure of the endophilin-A1 BAR domain. *J Mol Biol* 351: 653–661

Wenk MR, De Camilli P (2004) Protein-lipid interactions and phosphoinositide metabolism in membrane traffic: insights from vesicle recycling in nerve terminals. *Proc Natl Acad Sci USA* 101: 8262–8269

Yamagishi A, Masuda M, Ohki T, Onishi H, Mochizuki N (2004) A novel actin-bundling/filopodium-forming domain conserved in insulin receptor tyrosine kinase substrate p53 and missing in metastasis protein. *J Biol Chem* 279: 14929–14936

Zimmerberg J, Kozlov MM (2006) How proteins produce cellular membrane curvature. *Nat Rev Mol Cell Biol* 7: 9–19

nature medicine

# Monolayered mesenchymal stem cells repair scarred myocardium after myocardial infarction

Yoshinori Miyahara[1,9], Noritoshi Nagaya[1,9], Masaharu Kataoka[1], Bobby Yanagawa[1], Koichi Tanaka[1], Hiroyuki Hao[2], Kozo Ishino[3], Hideyuki Ishida[4], Tatsuya Shimizu[5], Kenji Kangawa[6], Shunji Sano[3], Teruo Okano[5], Soichiro Kitamura[7] & Hidezo Mori[8]

Mesenchymal stem cells are multipotent cells that can differentiate into cardiomyocytes and vascular endothelial cells. Here we show, using cell sheet technology, that monolayered mesenchymal stem cells have multipotent and self-propagating properties after transplantation into infarcted rat hearts. We cultured adipose tissue–derived mesenchymal stem cells characterized by flow cytometry using temperature-responsive culture dishes. Four weeks after coronary ligation, we transplanted the monolayered mesenchymal stem cells onto the scarred myocardium. After transplantation, the engrafted sheet gradually grew to form a thick stratum that included newly formed vessels, undifferentiated cells and few cardiomyocytes. The mesenchymal stem cell sheet also acted through paracrine pathways to trigger angiogenesis. Unlike a fibroblast cell sheet, the monolayered mesenchymal stem cells reversed wall thinning in the scar area and improved cardiac function in rats with myocardial infarction. Thus, transplantation of monolayered mesenchymal stem cells may be a new therapeutic strategy for cardiac tissue regeneration.

Myocardial infarction, a main cause of heart failure, leads to loss of cardiac tissue and impairment of left ventricular function. Therefore, restoring the scarred myocardium is desirable for the treatment of heart failure. Although needle injections of bone marrow cells into the myocardium have been performed for cardiac regeneration[1–5], it is difficult to reconstruct sufficient cardiac mass in the thinned scar area after myocardial infarction.

Recently, our colleagues have developed cell sheets using temperature-responsive culture dishes[6]. These cell sheets allow for cell-to-cell connections and maintain the presence of adhesion proteins because enzymatic digestion is not needed[7–10]. Therefore, cell sheet transplantation may be a promising strategy for partial cardiac tissue reconstruction. Skeletal myoblasts, fetal cardiomyocytes and embryonic stem cells have been considered as candidates for an implantable cell source[11–13]. It is difficult, however, to produce a multilayered construct requiring a vascular network. Thus, autologous somatic stem cells with self-propagating properties that can induce angiogenesis are a desirable cell source for a transplantable sheet.

Mesenchymal stem cells (MSCs) are multipotent adult stem cells that reside within the bone marrow microenvironment[14,15]. MSCs can differentiate not only into osteoblasts, chondrocytes, neurons and skeletal muscle cells, but also into vascular endothelial cells[16] and cardiomyocytes[17–20]. In contrast to their hematopoietic counterparts, MSCs are adherent and can expand in culture. Recently, MSCs have been isolated from adipose tissue[21–24], which is typically abundant in individuals with cardiovascular disease. Here, we investigated the therapeutic potency of monolayered MSCs derived from adipose tissue using cell sheet technology.

## RESULTS

### Characteristics of adipose tissue–derived MSCs

We isolated MSCs from subcutaneous adipose tissue of male Sprague-Dawley rats on the basis of the adherent properties of these cells. We obtained $1.7 \times 10^5 \pm 0.2 \times 10^5$ cells from 1 g adipose tissue in a 12-h culture. By day 4 of culture of the minced adipose tissue, spindle-shaped adherent cells were apparent and formed symmetric colonies. After approximately three to four passages, most adherent cells expressed CD29 and CD90 (**Supplementary Fig. 1** online). In contrast, the majority of adherent cells were negative for CD34 and CD45. They were also negative for CD31, a marker for vascular endothelial cells, and negative for α smooth muscle actin (αSMA), a marker for smooth muscle cells. A small fraction of adherent cells expressed CD71, CD106 and CD117. These results were similar to those from bone marrow–derived MSCs[15,22,25] (**Supplementary Fig. 1** online). Using previously described methods[16,22,26], we confirmed that these adipose-derived adherent cells, like bone marrow–derived MSCs, were multipotent, as judged by their ability to differentiate into adipocytes, osteoblasts and vascular endothelial cells. Thus, we

[1]Department of Regenerative Medicine and Tissue Engineering, National Cardiovascular Center Research Institute and [2]Department of Pathology, National Cardiovascular Center, 5-7-1 Fujishirodai, Suita, Osaka, 565-8565, Japan. [3]Department of Cardiovascular Surgery, Okayama University Graduate School of Medicine, Dentistry and Pharmaceutical Sciences, 2-5-1 Shikata-cho, Okayama, 700-8555, Japan. [4]Department of Physiology, School of Medicine, Tokai University, Bohseidai, Isehara, Kanagawa, 259-1193, Japan. [5]Institute of Advanced Biomedical Engineering and Science, Tokyo Woman's Medical University, 8-1 Kawada-cho, Shinjuku-ku, Tokyo, 162-8666, Japan. [6]Department of Biochemistry, National Cardiovascular Center Research Institute and [7]Department of Cardiovascular Surgery, National Cardiovascular Center and [8]Department of Cardiac Physiology, National Cardiovascular Center Research Institute, 5-7-1 Fujishirodai, Suita, Osaka, 565-8565, Japan. [9]These authors contributed equally to this work. Correspondence should be addressed to N.N. (nnagaya@ri.ncvc.go.jp) or H.M. (hidemori@ri.ncvc.go.jp).

Received 9 August 2005; accepted 3 March 2006; published online 2 April 2006; doi:10.1038/nm1391

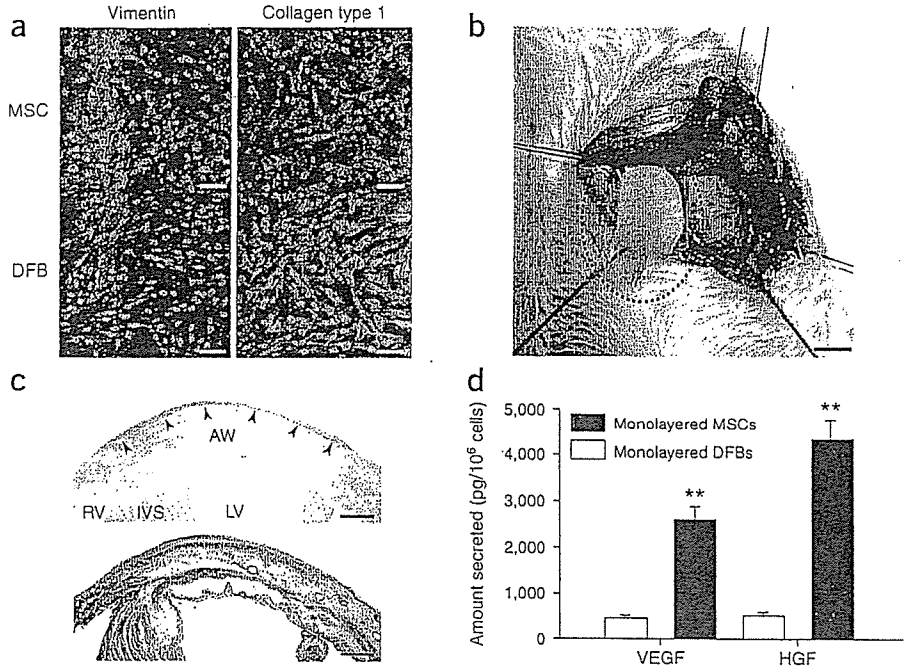


Figure 2 Characteristics of monolayered MSCs. (a) Properties of constituent cells in the monolayered grafts. Compared with DFBs (green), MSCs (green) are positive for vimentin (red) and slightly positive for collagen type 1 (red). (b) Monolayered MSCs (in the dotted circle) transferred to the infarcted heart. (c) Extent of monolayered MSCs 48 h after transplantation (arrows). AW, anterior wall; LV, left ventricle; RV right ventricle; IVS, interventricular septum. (d) Comparison of secretion of growth factors between monolayered MSCs and DFBs. $^{**}P < 0.01$ versus DFBs. Scale bar in a, 20 μm; in b, 5 mm; in c, 100 μm.

before transplantation (Fig. 2a and Supplementary Fig. 1 online), suggesting that the MSC tissue includes a number of undifferentiated MSCs. Taken together, the grown MSC tissue was composed of newly formed blood vessels, undifferentiated MSCs and few cardiomyocytes.

### Fluorescence *in situ* hybridization analysis

We performed fluorescence *in situ* hybridization (FISH) to detect X and Y chromosomes after sex-mismatched transplantation of monolayered MSCs. We transplanted GFP-expressing monolayered MSCs derived from male rats to female Sprague-Dawley rats that had suffered an infarct. Four weeks later, newly formed cardiomyocytes that were positive for GFP had only one set of X and Y chromosomes, whereas we detected two X chromosomes exclusively in $GFP^-$ host-derived cells (Fig. 4h). We counted the X and Y chromosomes in male and female control rats and in the MSC sheet–transplanted rats (Supplementary Table 2 online), and we did not detect extra copies of the X or Y chromosome in graft-derived $GFP^+$ cardiomyocytes. When we compared the frequencies of the occurrence of zero, one, two and more than two X chromosomes in the $GFP^+$ cardiomyocytes with the frequencies in male control cardiomyocytes, the $GFP^+$ cardiomyocytes did not show an increased proportion of X chromosomes ($0.25 > P > 0.10$, $\chi^2$ test).

### Effects of monolayered MSCs on cardiac function

Heart failure developed 8 weeks after coronary ligation, as indicated by an increase in left ventricle end-diastolic pressure (LVEDP) and attenuation of maximum and minimum rate of change in left ventricular pressure ($dP/dt$). Autologous transplantation of monolayered MSCs, however, resulted in decreased LVEDP (Fig. 5a). Left ventricle maximum and minimum $dP/dt$ were significantly improved in the MSC group (Fig. 5b,c). We did not observe these hemodynamic improvements in the DFB group. The MSC group also had significantly lower right ventricular weight and lung weight than the DFB and untreated groups 4 weeks after transplantation (Supplementary Table 1 online). These results suggest that transplantation of monolayered MSCs has beneficial hemodynamic effects in rats with chronic heart failure.

Echocardiographic analysis showed that transplantation of monolayered MSCs significantly increased diastolic thickness of the infarcted anterior wall (Fig. 5d). Left ventricle end-diastolic dimension at 8 weeks was significantly smaller in the MSC group than in the DFB and untreated groups (Fig. 5e). Transplantation of the monolayered MSCs significantly increased left ventricle fractional shortening (Fig. 5f). Left ventricle wall stress in diastole was markedly lower in the MSC group than in the DFB and untreated groups (Supplementary Table 3 online). Plasma atrial natriuretic peptide (ANP) in the DFB and untreated groups was markedly elevated 8 weeks after myocardial infarction (Fig. 5g). Transplantation of the monolayered MSCs inhibited the increase in plasma ANP.

### Survival analysis

The Kaplan-Meier survival curve showed that 4-week survival after coronary ligation did not differ significantly between the untreated and MSC groups before transplantation (Fig. 5h). Notably, however, no rats died after transplantation of monolayered MSCs. Therefore, the survival rate after transplantation was markedly higher in the MSC group than in the untreated group (4-week survival after transplantation was 100% for the MSC group versus 71% for the untreated group, log-rank test, $P < 0.05$).

## DISCUSSION

There are several advantages to monolayered MSC transplantation. First, the self-propagating property of MSCs *in situ* leads to the formation of a thick stratum on the surface of the scarred myocardium. Second, the multipotency of MSCs and their ability to supply angiogenic cytokines allows neovascularization in the MSC tissue. Third, the reconstruction of thick myocardial tissue reduces left ventricle wall stress and results in improvement of cardiac function after myocardial infarction. Finally, a substantial part of the transplanted tissue is composed of undifferentiated MSCs, and it is tempting to speculate that such cells may act against future progressive left ventricle remodeling.

Cellular cardiomyoplasty using needle injections is emerging as a treatment option for individuals with chronic heart failure, but it may be limited by failure to regenerate cardiac mass. The cell sheet allows for cell-to-cell connections owing to the lack a need for enzymatic digestion[6–10]. Thus, the cell sheet has attracted considerable interest as a tool for tissue engineering[28]. Here, we used adipose tissue–derived MSCs as a cellular source for the cell sheet, which resulted in successful autologous transplantation in heterogenic rats without immunological

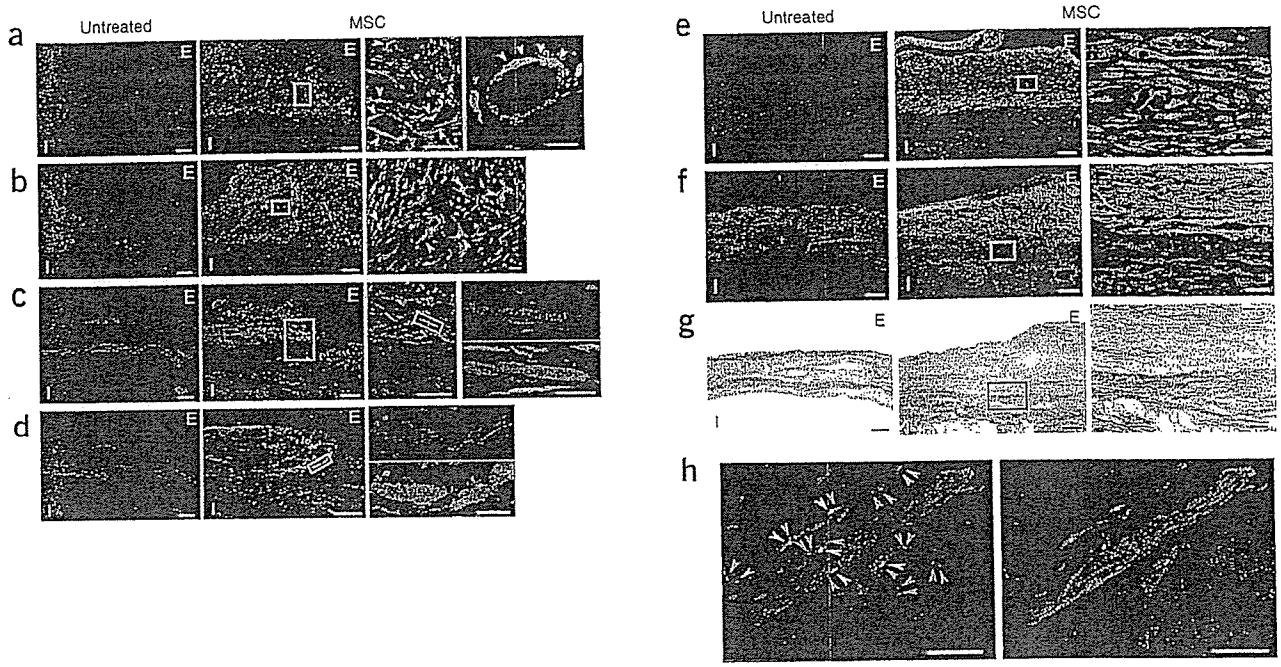


Figure 4 Differentiation of MSCs within the MSC tissue after growth *in situ*. (a,b) GFP-expressing MSCs (green) were identified as a thick stratum at the epicardial side of the myocardium. The MSC tissue contained a number of vascular structures positive for vWF (red, a) and αSMA (red, b). MSCs that did not participate in blood vessel formation were only rarely positive for αSMA, a marker for myofibroblasts. Arrows indicate transplanted MSCs positive for vWF or αSMA. (c,d) Some MSCs within the MSC tissue were positive for cardiac markers cardiac troponin T (red, c) and desmin (red, d). (e) Most of the MSC tissue was positive for vimentin (red). (f) The MSC tissue modestly stained for collagen type 1 (red). (g) Collagen deposition was also detected by picrosirius red staining. (h) FISH analysis. Newly formed cardiomyocytes (desmin, red) that were positive for GFP (green) had only one set of X (purple) and Y chromosomes (white), whereas two X chromosomes were detected exclusively in $GFP^-$ host-derived cells. Nuclei are stained with DAPI (blue, a–f and h). Scale bars in left three panels of a and c and in two left panels of b and d–g, 100 μm; in h and far right panels of a–g, 20 μm. E, epicardial side; I, intimal side.

In summary, adipose tissue–derived monolayered MSCs can be readily engrafted to the scarred myocardium, grow gradually *in situ* and become a thick stratum that includes newly formed vessels, cardiomyocytes and undifferentiated MSCs. The engrafted MSCs reversed wall thinning in the scar area and improved cardiac function and survival in rats with myocardial infarction. Thus, transplantation of monolayered MSCs may be a new therapeutic strategy for cardiac tissue regeneration.

## METHODS

**Model of heart failure.** All protocols were performed in accordance with the guidelines of the Animal Care Ethics Committee of the Japanese National Cardiovascular Center Research Institute. We used male Sprague-Dawley rats (Japan SLC) weighing 187–215 g. A myocardial infarction model was produced by ligation of the left coronary artery, as described previously[30]. Briefly, we anesthetized rats with sodium pentobarbital (30 mg/kg) and ventilated them with a volume-regulated respirator. We exposed hearts by left thoracotomy, and ligated the left coronary artery 2–3 mm from its origin between the pulmonary artery conus and the left atrium with a 6-0 Prolene suture. The sham group underwent thoracotomy and cardiac exposure without coronary ligation. The surviving rats were maintained on standard rat chow.

**Study protocol.** We randomly placed rats into four groups: rats with chronic heart failure that underwent transplantation of monolayered MSCs (MSC group; $n = 12$), rats with chronic heart failure given monolayered DFBs (DFB group; $n = 12$), rats with chronic heart failure without transplantation (untreated group; $n = 12$) and sham-operated rats without transplantation (sham group; $n = 10$). Four weeks after coronary ligation, the MSC and DFB groups underwent autologous transplantation of each monolayered cell graft onto the anterior wall, including the scar area (**Supplementary Methods** online). The other two groups underwent the same operative procedures without transplantation. We performed hemodynamic studies, echocardiography and histological assessments 4 and 8 weeks after coronary ligation (**Supplementary Methods**). Upon killing at 8 weeks after coronary ligation, only those rats with infarct size > 25% of the left ventricle area were included in this study. Therefore, the variation in infarct size between the experimental rats was relatively low (28–41%, average 33.9% ± 1.9%).

**Isolation and culture of MSCs from adipose tissue.** Immediately after coronary ligation, we acquired subcutaneous adipose tissue (1.1 ± 0.1 g) from the right inguinal region of each rat. We minced adipose tissue with scissors and digested it with 10 ml of type 1 collagenase solution (0.1 mg/ml, Worthington Biochemical) for 1 h in a 37 °C water bath shaker. After filtration with mesh filter (Costar 3480, Corning) and centrifugation at 780*g* for 8 min, we suspended isolated cells in α-MEM supplemented with 10% FCS and antibiotics, plated them onto a 100-mm dish and incubated them at 37 °C with 5% $CO_2$. A small number of spindle-shaped cells were apparent in visible symmetric colonies by days 5–7.

**Preparation of temperature-responsive dishes.** Specific procedures for preparation of square-designed PIPAAm-grafted dishes have been previously described[9]. Briefly, we spread IPAAm monomer (Kohjin) in 2-propanol solution onto 60-mm polystyrene culture dishes (Corning). We then subjected the dishes to irradiation (0.25-MGy electron beam dose) using an Area Beam Electron Processing system (Nisshin High-Voltage) to immobilize IPAAm on the dish surface; we then rinsed dishes with cold distilled water and dried them in nitrogen gas. In the second step, we masked the PIPAAm-grafted surface with a square glass coverslip (24 × 24 mm, Matsunami Glass). We spread acrylamide (AAm) monomer solution in 2-propanol onto the masked dish surface. We then irradiated the dish surface with an electron beam and washed it. As a result, the central square area of each dish was PIPAAm grafted (temperature responsive), and the surrounding border was poly-AAm grafted (non–cell adhesive). This PIPAAm-grafted surface is hydrophobic under culture

12. Skobel, E. *et al.* Transplantation of fetal cardiomyocytes into infarcted rat hearts results in long-term functional improvement. *Tissue Eng.* 10, 849–864 (2004).
13. Hodgson, D.M. *et al.* Stable benefit of embryonic stem cell therapy in myocardial infarction. *Am. J. Physiol. Heart Circ. Physiol.* 287, H471–H479 (2004).
14. Makino, S. *et al.* Cardiomyocytes can be generated from marrow stromal cells in vitro. *J. Clin. Invest.* 103, 697–705 (1999).
15. Pittenger, M.F. *et al.* Multilineage potential of adult human mesenchymal stem cells. *Science* 284, 143–147 (1999).
16. Reyes, M. *et al.* Origin of endothelial progenitors in human postnatal bone marrow. *J. Clin. Invest.* 109, 337–346 (2002).
17. Toma, C., Pittenger, M.F., Cahill, K.S., Byrne, B.J. & Kessler, P.D. Human mesenchymal stem cells differentiate to a cardiomyocyte phenotype in the adult murine heart. *Circulation* 105, 93–98 (2002).
18. Wang, J.S. *et al.* Marrow stromal cells for cellular cardiomyoplasty: feasibility and potential clinical advantages. *J. Thorac. Cardiovasc. Surg.* 120, 999–1005 (2000).
19. Jiang, Y. *et al.* Pluripotency of mesenchymal stem cells derived from adult marrow. *Nature* 418, 41–49 (2002).
20. Nagaya, N. *et al.* Transplantation of mesenchymal stem cells improves cardiac function in a rat model of dilated cardiomyopathy. *Circulation* 112, 1128–1135 (2005).
21. Rangappa, S., Fen, C., Lee, E.H., Bongso, A. & Wei, E.S. Transformation of adult mesenchymal stem cells isolated from the fatty tissue into cardiomyocytes. *Ann. Thorac. Surg.* 75, 775–779 (2003).
22. Zuk, P.A. *et al.* Human adipose tissue is a source of multipotent stem cells. *Mol. Biol. Cell* 13, 4279–4295 (2002).
23. Gaustad, K.G., Boquest, A.C., Anderson, B.E., Gerdes, A.M. & Collas, P. Differentiation of human adipose tissue stem cells using extracts of rat cardiomyocytes. *Biochem. Biophys. Res. Commun.* 314, 420–427 (2004).
24. Planat-Benard, V. *et al.* Plasticity of human adipose lineage cells toward endothelial cells: physiological and therapeutic perspectives. *Circulation* 109, 656–663 (2004).
25. Lee, R.H. *et al.* Characterization and expression analysis of mesenchymal stem cells from human bone marrow and adipose tissue. *Cell. Physiol. Biochem.* 14, 311–324 (2004).
26. Li, J., Takaishi, K., Cook, W., McCorkle, S.K. & Unger, R.H. Insig-1 "brakes" lipogenesis in adipocytes and inhibits differentiation of preadipocytes. *Proc. Natl. Acad. Sci. USA* 100, 9476–9481 (2003).
27. Vande Berg, J.S., Rudolph, R. & Woodward, M. Comparative growth dynamics and morphology between cultured myofibroblasts from granulating wounds and dermal fibroblasts. *Am. J. Pathol.* 114, 187–200 (1984).
28. Nishida, K. *et al.* Corneal reconstruction with tissue-engineered cell sheets composed of autologous oral mucosal epithelium. *N. Engl. J. Med.* 351, 1187–1196 (2004).
29. Shimizu, T., Yamato, M., Kikuchi, A. & Okano, T. Cell sheet engineering for myocardial tissue reconstruction. *Biomaterials* 24, 2309–2316 (2003).
30. Nishikimi, T., Uchino, K. & Frohlich, E.D. Effects of α1-adrenergic blockade on intrarenal hemodynamics in heart failure rats. *Am. J. Physiol. Regul. Integr. Comp. Physiol.* 262, R198–R203 (1998).

Available online at www.sciencedirect.com
ScienceDirect
Biochemical and Biophysical Research Communications 349 (2006) 1242–1249
BBRC
www.elsevier.com/locate/ybbrc

# Beraprost sodium enhances neovascularization in ischemic myocardium by mobilizing bone marrow cells in rats

Yoshinori Miyahara [a], Shunsuke Ohnishi [a], Hiroaki Obata [a], Kozo Ishino [b], Shunji Sano [b], Hidezo Mori [c], Kenji Kangawa [d], Soichiro Kitamura [e], Noritoshi Nagaya [a,*]

[a] *Department of Regenerative Medicine and Tissue Engineering, National Cardiovascular Center Research Institute, Osaka, Japan*
[b] *Department of Cardiovascular Surgery, Okayama University Graduate School of Medicine, Dentistry and Pharmaceutical Sciences, Okayama, Japan*
[c] *Department of Cardiac Physiology, National Cardiovascular Center Research Institute, Osaka, Japan*
[d] *Department of Biochemistry, National Cardiovascular Center Research Institute, Osaka, Japan*
[e] *Department of Cardiovascular Surgery, National Cardiovascular Center, Osaka, Japan*

Received 13 August 2006
Available online 7 September 2006

**Abstract**

Beraprost sodium, an orally active prostacyclin analogue, has vasoprotective effects such as vasodilation and antiplatelet activities. We investigated the therapeutic potential of beraprost for myocardial ischemia. Immediately after coronary ligation of Sprague–Dawley rats, beraprost (200 μg/kg/day) or saline was subcutaneously administered for 28 days. Four weeks after coronary ligation, administration of beraprost increased capillary density in ischemic myocardium, decreased infarct size, and improved cardiac function in rats with myocardial infarction. Beraprost markedly increased the number of CD34-positive cells and c-kit-positive cells in plasma. Also, four weeks after coronary ligation of chimeric rats with GFP-expressing bone marrow, bone marrow-derived cells were incorporated into the infarcted region and its border zone. Treatment with beraprost increased the number of GFP/von Willebrand factor-double-positive cells in the ischemic myocardium. These results suggest that beraprost has beneficial effects on ischemic myocardium partly by its ability to enhance neovascularization in ischemic myocardium by mobilizing bone marrow cells.


*Keywords:* Prostacyclin analogue; Myocardial infarction; Neovascularization; Bone marrow mobilization

Interruption of myocardial blood flow leads to rapid death of cardiomyocytes and vascular structures, resulting in the development of heart failure [1]. Stem or progenitor cells are mobilized from bone marrow into the peripheral blood in response to tissue ischemia, migrate to sites of injured tissues, and differentiate into endothelial cells and cardiomyocytes [2–4]. However, the compensatory mechanisms are insufficient to heal infarcted myocardium. Earlier studies have shown that bone marrow cells artificially mobilized by cytokines repair the infarcted heart and improve cardiac function after acute myocardial infarction [5,6]. Therefore, enhancement of bone marrow cell mobilization leading to neovascularization following revascularization would be beneficial for the treatment of acute myocardial infarction.

Beraprost sodium (BPS) is a chemically stable prostacyclin analogue owing to its cyclo-pentabenzofuranyl structure [7]. It has been well established that BPS has vasoprotective effects such as vasodilation and antiplatelet activities [8–11]. Thus, BPS has been used in the treatment of peripheral arterial disease [12,13] and pulmonary arterial hypertension [14,15]. Although a limited number of studies suggest therapeutic potential of prostacyclin for the treatment of myocardial ischemia [16–18], the underlying mechanisms still remain unclear. In addition, little information is available regarding the therapeutic potential of prostacyclin analogues such as BPS for myocardial ischemia. A recent study has shown that BPS activates endothelial

* Corresponding author. Fax: +81 6 6833 9865.
*E-mail address:* nnagaya@ri.ncvc.go.jp (N. Nagaya).

0006-291X/$ - see front matter © 2006 Elsevier Inc. All rights reserved.
doi:10.1016/j.bbrc.2006.08.178

nitric oxide synthase (eNOS) through the c-AMP/protein kinase A pathway [19]. Activation of eNOS is known to contribute to bone marrow cell mobilization, leading to neovascularization [20]. These results raise the possibility that BPS may have beneficial effects on the ischemic myocardium through enhancement of bone marrow cell mobilization.

Thus, the purposes of this study were: (1) to examine the effect of BPS on mobilization and recruitment of bone marrow cells after acute myocardial infarction, (2) to investigate whether BPS induces neovascularization in the ischemic myocardium, and (3) to investigate whether treatment with BPS improves cardiac function in rats with myocardial infarction.

## Methods

*Model of myocardial infarction.* We used male Sprague–Dawley rats (Japan SLC Inc., Hamamatsu, Japan) weighing 185–215 g. Myocardial infarction was produced by left coronary ligation, as described previously [21]. Briefly, after rats were anesthetized with sodium pentobarbital (30 mg/kg), they were artificially ventilated with a volume-regulated respirator. The heart was exposed via a left thoracotomy incision. Then, the left coronary artery was ligated 2–3 mm from its origin between the pulmonary artery conus and the left atrium with a 6-0 Prolene suture. Finally, the heart was restored to its normal position, and the chest was closed. Experimental protocols were performed in accordance with the "Guidelines of the Animal Care Ethics Committee of the National Cardiovascular Center Research Institute", which complies NIH Guidelines.

*Administration of BPS.* Immediately after coronary ligation, BPS (200 μg/kg/day, Astellas Pharma Inc., Tokyo, Japan) was subcutaneously administered to surviving rats using an osmotic mini-pump for 4 weeks (BPS group, $n = 12$). As a control, saline was similarly administered to rats receiving coronary ligation (Control group, $n = 12$).

*Echocardiographic studies.* Echocardiographic studies were performed 4 weeks after coronary ligation. M-mode tracings were obtained at the level of the papillary muscles using an echocardiographic system equipped with a 7.5-MHz phased-array transducer (HP SONOS 5500; Hewlett Packard Co., Andover, MA). Anterior and posterior end-diastolic and end-systolic wall thickness, LV end-diastolic and end-systolic dimensions, and LV fractional shortening were measured by the American Society for Echocardiography leading-edge method in three consecutive cardiac cycles. LV meridional wall stress was estimated as $0.344 \times \text{LV pressure} \times \{\text{LV dimension}/(1 + \text{PWT/LV dimension})\}$, where PWT is posterior wall thickness [22].

*Hemodynamic studies.* Hemodynamic studies were performed 4 weeks after coronary ligation, following echocardiography. After anesthesia with pentobarbital sodium, a 1.5F micromanometer-tipped catheter (Millar Instruments Inc., Houston, TX) was advanced into the LV through the right common carotid artery. Hemodynamic variables were measured with a pressure transducer connected to a polygraph. After completion of these measurements, the left and right ventricles and the lungs were excised and weighed. Infarct size was determined as a percentage of the entire LV area ($n = 5$ in each group), as reported previously [23]. Briefly, incisions were made in the posterior LV so that the tissue could be pressed flat. The circumference of the entire flat LV and of the visualized infarcted area, as judged from both the epicardial and endocardial sides, was outlined on a clear plastic sheet. The difference in weight between the two marked areas on the sheet was used to determine infarct size and was expressed as a percentage of LV surface area.

*Measurement of plasma ANP level.* Blood samples were obtained 4 weeks after coronary ligation. Plasma atrial natriuretic peptide (ANP), a marker for heart failure, was measured by enzyme immunoassay (Peninsula Laboratories Inc., San Carlos, CA).

*Mononuclear cell mobilization and FACS analysis.* To investigate whether administration of BPS mobilizes bone marrow cells, an additional 12 rats were randomized to receive BPS (200 μg/kg/day, BPS group, $n = 6$) or saline (Control group, $n = 6$). On the third day of BPS or saline treatment, 4 ml of blood was drawn from the inferior vena cava of each rat. Peripheral blood was obtained at the end of infusion. After mononuclear cells were counted, they were incubated for 30 min at 4 °C with fluorescein isothiocyanate (FITC)-conjugated mouse monoclonal antibodies against rat CD34 (clone ICO-115, Santa Cruz) and CD45 (clone OX-1), and FITC-conjugated rabbit anti-rat c-Kit polyclonal antibody (clone C-19, Santa Cruz). Immunofluorescence-labeled cells were analyzed by quantitative flow cytometry with a FACSCalibur flow cytometer (BD Biosciences, Mountain View, CA). Isotype-identical antibodies served as controls.

*RT-PCR assay.* To investigate whether bone marrow cells express the prostacyclin receptor (IP receptor), we analyzed expression of its mRNA by reverse transcription-polymerase chain reaction (RT-PCR). In brief, total RNA of bone marrow cells was extracted with guanidine isothiocyanate (RNeasy Mini Kit, Qiagen). Then, reverse-transcribed single-stranded cDNA was subjected to PCR (PCR Amplification Kit, Takara) using primer sets for the IP receptor (Hokkaido System Science Co., Ltd., Sapporo, Japan, forward, 5′-GGCACGAGAGGATGAAGTTTACC-3′; reverse, 5′-GTCAGAGGCACAGCAGTCAATGG-3′) and G3PDH (Clonetech Laboratories Inc., Mountain View, CA, forward, 5′-TG AAGGTCGGTGTCAACGGATTTGGC-3′; reverse, 5′-CATGTAGG CCATGAGGTCCACCAC-3′).

*Creation of bone marrow-chimeric rats.* To assess recruitment of bone marrow cells after BPS administration, bone marrow transplantation was performed by using male normal Sprague–Dawley rats as recipients and male Green fluorescent protein (GFP)-transgenic rats (SD-Tg [Act-EGFP] CZ-004Osb, Japan SLC Inc.) as donors, using a previously described method [24]. Briefly, bone marrow was harvested by flushing the cavity of femurs and tibias from GFP-transgenic rats with phosphate-buffered saline. Then, $3 \times 10^7$ GFP-positive bone marrow cells were individually administered to 12 lethally irradiated (900c Gray) rats via the tail vein. Four weeks after transplantation, flowcytometric analysis determined that 90% of peripheral blood mononuclear cells from both donors and 8 of 12 chimeric rats were GFP-positive, suggesting the establishment of stable chimerism. These chimeric rats were subjected to left coronary ligation, followed by administration of BPS (200 μg/kg/day, BPS group, $n = 4$) or saline (Control group, $n = 4$) using an osmotic mini-pump for 4 weeks.

*Histological examination.* To detect fibrosis in the cardiac muscle, the LV myocardium ($n = 5$, each group) was fixed in 10% formalin, cut transversely in three sections, embedded in paraffin, and stained with Masson's trichrome. To detect capillary endothelial cells in the peri-infarct area, we performed DAB staining (LSAB2 System HRP, Dako Cytomation Co., Denmark) using rabbit polyclonal anti-von Willebrand factor (vWF) antibody (Dako). A total of 10 different fields from three different sections were randomly selected, and the number of capillaries was counted in the peri-infarct area using a light microscope at 200× magnification. Capillary density was expressed as the mean number of capillaries per square millimeter. Also, 4 weeks after coronary ligation in bone marrow-chimeric rats ($n = 4$ in each group), the LV myocardium was excised, embedded in OCT compound, snap-frozen in liquid nitrogen, and cut transversely into 6-μm-thick sections from base to apex. Immunofluorescent staining was performed using rabbit polyclonal anti-vWF antibody (Dako), mouse monoclonal anti-cardiac troponin T antibody (Neomarkers, Fremont, CA), and rabbit polyclonal Alexa 488-conjugated anti-GFP antibody (Molecular Probes Inc., Eugene, OR). The nuclei were counterstained with 4′,6′-diamidino-2-phenylindole (DAPI). We measured the number of GFP/vWF-double-positive cells incorporated into vascular structures in 10 randomly selected fields in the peri-infarct area per section in a blinded fashion using a fluorescence microscope.

*Statistical analysis.* Numerical values are expressed as means ± SEM. Comparisons of parameters between two groups were made by unpaired Student's $t$ test. A value of $p < 0.05$ was considered significant.

## Results

### *Cardiac structure*

Body weight at 4 weeks after coronary ligation was significantly greater in the BPS group than in the Control group (Table 1). Right ventricular weight and lung weight in the BPS group were significantly smaller than those in the Control group, although LV weight did not differ between the two groups. Moderate to large infarcts were observed in the Control group (Fig. 1A). However, administration of BPS significantly decreased infarct size in rats with myocardial infarction (Fig. 1A and B). BPS significantly decreased LV end-diastolic dimension (LVDD) (Fig. 1C).

Table 1
Physiological profiles of experimental groups

| | Control | BPS |
|---|---|---|
| Number | 12 | 12 |
| Body weight (g) | | |
| Baseline | 198 ± 3 | 204 ± 3 |
| After treatment | 319 ± 6 | 352 ± 9* |
| LV wt/body wt (g/kg) | 2.28 ± 0.04 | 2.27 ± 0.04 |
| RV wt/body wt (g/kg) | 0.99 ± 0.05 | 0.61 ± 0.02** |
| Lung wt/body wt (g/kg) | 6.55 ± 0.62 | 3.88 ± 0.1** |
| Plasma AND level (pg/ml) | 798 ± 99 | 498 ± 57* |

Control, infarct rats without treatment; BPS, infarct rats treated with BPS administration; AND, atrial natriuretic protein. Data are expressed as means ± SEM. $^{*}p < 0.05$, $^{**}p < 0.01$ vs. Control group.

### *Cardiac function*

Neither heart rate nor mean arterial pressure differed between the BPS and Control groups (Table 2). LV fractional shortening and LV maximum d$P$/d$t$ in the BPS group were significantly greater than those in the Control group (Fig. 2A and B). LV end-diastolic pressure (LVEDP) in the BPS group was significantly lower than that in the Control group (Fig. 2C). LV minimum d$P$/d$t$ was also improved by BPS (Fig. 2D). Treatment with BPS attenuated the increase in plasma ANP level after myocardial infarction (Table 1). BPS significantly increased anterior wall thickening, although it did not significantly alter posterior wall thickening (Table 2). Thickness of the anterior and posterior walls tended to be greater in the BPS group, but these changes did not reach statistical significance. LV diastolic wall stress in the BPS group was significantly lower than that in the Control group.

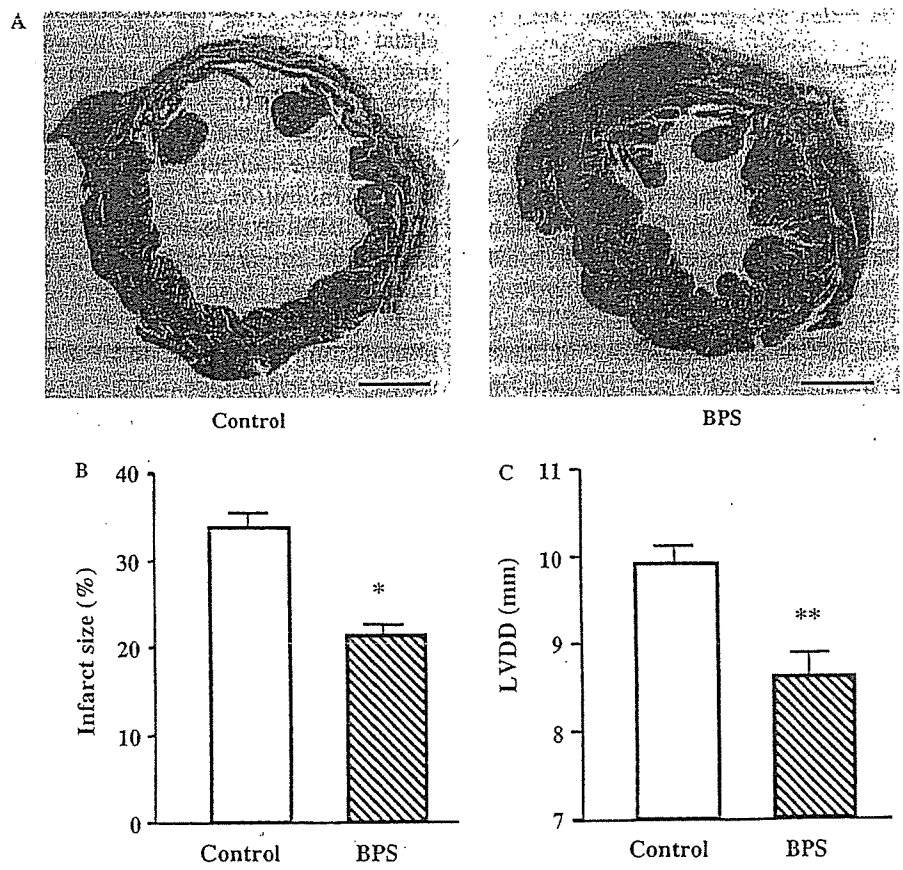


Fig. 1. (A) Representative examples of Masson's trichrome staining of transverse sections of LV myocardium 4 weeks after coronary ligation. Scale bars = 2 mm. (B,C) Quantitative analysis of infarct size and LV end-diastolic dimension (LVDD). Infarcted area and LVDD in the BPS group were significantly smaller than those in the Control group. Data are expressed as means ± SEM. $^{*}p < 0.05$, $^{**}p < 0.01$ vs. Control group.